δ-Bonding versus Electron Localization in Formally Divalent Rare Earth Complexes

Ross E. MacKenzie,[1,2] Tomáš Hajdu,[2] John A. Seed,[1,2] George F. S. Whitehead,[2] Ralph W. Adams,[2] Nicholas F. Chilton,[2,3] David Collison,[2] Eric J. L. McInnes,[2] Conrad A. P. Goodwin*[1,2]

[1] Centre for Radiochemistry Research, The University of Manchester, Oxford Road, Manchester, M13 9PL (UK).

[2] Department of Chemistry, The University of Manchester, Oxford Road, Manchester, M13 9PL (UK).

[3] Research School of Chemistry, The Australian National University, Sullivans Creek Road, Canberra, 2601 (Australia).

*Correspondence: conrad.goodwin@manchester.ac.uk

Abstract

Herein we present a series of room-temperature stable, structurally analogous rare-earth complexes of the form [M(NHAr$^{i\text{Pr6}}$)$_2$] (M = Sc, Y, La, Sm, Eu, Tm, Yb; NHAr$^{i\text{Pr6}}$ = {N(H)C$_6$H$_3$-2,6-(C$_6$H$_2$-2,4,6-*i*Pr$_3$)$_2$}). All seven complexes contain formal M(II) ions with close M···arene contacts. The Sc(II) and La(II) complexes display an open-book deformation (*ca*. 11–13°) of one metal-bound arene, while for Y(II) there are two symmetry-equivalent Y···arene interactions with smaller deformations (*ca*. 7°). In the case of Sc(II), Y(II), and La(II), quantum chemical calculations reveal the delocalization of a metal *d*-electron from M(II) into ligand π-orbitals forming δ-bonding interactions. In the case of Y(II), EPR and UV-Vis-NIR spectroscopies combined with quantum chemical calculations show a structural change in solution to the single-open-book deformation structure in common with Sc(II) and La(II). While the Sm(II), Eu(II), Tm(II), and Yb(II) complexes retain similar close M···arene contacts, their 4*f*$^{n+1}$ valence electron configurations do not lead to δ-bonding interactions; however, NMR studies of diamagnetic 4*f*^{14} Yb(II) reveal ^{171}Yb···^{1}H coupling to arene ring-protons at room temperature and show that the M···arene interaction is preserved in solution across a wide temperature range. These complexes represent a rare structurally analogous M(II) series which extends from the group 3 elements into the lanthanide series and includes an extremely rare neutral formal Sc(II) complex.

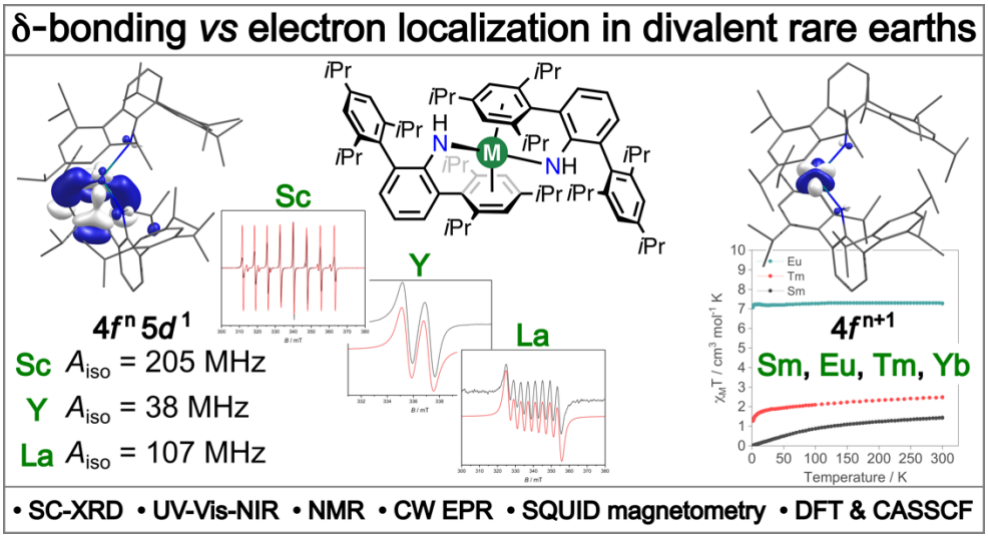

Introduction

Chemistry of the group three elements Sc, Y, La, along with the lanthanide elements Ce–Lu (collectively the rare earth elements) in oxidation states lower than M(III) has undergone a renaissance since the start of the 21st century (excluding radioactive Pm). Historically, the extent of low oxidation state molecular and solution-state chemistry for these elements was limited to that of Eu(II), Yb(II), and Sm(II),[1-4] and some find use in selective organic transformations.[5-7] These three divalent ions occupy privileged positions in the lanthanide (Ln) row: Eu(II) has a stable half-filled $4f^7$ configuration and a potential of –0.35 V (all values are *vs* NHE) for the $Eu^{3+/2+}$ couple, which is followed by $Yb^{3+/2+}$ at –1.15 V due to the stable filled $4f^{14}$ configuration of Yb(II), and then finally $Sm^{3+/2+}$ at –1.55 V due to the $4f^6$ configuration of Sm(II).[8] Beyond these, in order of increasingly negative formal reduction potential lies Tm(II) ($4f^{13}$, –2.3 V), Dy(II) (–2.5 V), and Nd(II) (–2.6 V).[8] All three are potent reductants, with Dy(II) and Nd(II) being capable of Birch-like reduction chemistry,[6,9,10] though they are isolable as simple coordination complexes (e.g. $[LnI_2(THF)_5]$).[1,10-13] Calculated reduction potentials for much of the rest of the lanthanide series place the $Ln^{3+/2+}$ couples at such negative potentials as to make them theoretically inaccessible in common solvents.[8,14-16]

More recently, a fuller appreciation for the role of ligand field effects on the vacant *d*-manifold and redox properties of the rare earth elements, coupled with judicious choice of molecular design, has helped overturn the *status quo*.[17] For example, while the 5*d* manifold is vacant in Ln(III) complexes, a suitable coordination environment as in $[Ln(Cp^R)_3]^-$ or $[Ln(Cp^R)_2]$ (Cp^R = η^5-$\{C_5R_5\}$, R = H, alkyl, or tri-alkyl-silyl groups), allows the isolation of complexes where a valence electron occupies a molecular orbital closely resembling an atomic orbital of *d*-parentage to give $4f^n5d^1$ or $4f^n\{5d/6s\}^1$ configurations.[18-33] That is except for the traditional divalent elements Sm, Eu and Yb,[25,27-38] which instead tend to possess $4f^{n+1}$ configurations

due to large $4f^{n+1} \rightarrow 4f^n5d^1$ promotional energies in the Ln(II) oxidation state.[39,40] Both Dy(II) and Nd(II) have been shown capable of giving either a $4f^{n+1}$ or a $4f^n$ $\{5d/6s\}^1$ configuration,[24,33,41,42] but note that these convenient formalisms don't necessarily reflect an accurate quantum chemical description of the electronic structure.[18] Still, they are useful to guide the design of new molecules in a chemically intuitive language. Leveraging the availability of 5*d* orbitals in Ln elements has recently allowed the isolation of molecules with formal Ln···Ln bonds,[26,43-45] which naturally follows from earlier observations of metal-metal bonding in solid-state halides.[14,43] Meanwhile, the physics of these systems provides opportunities for the design of novel qubit candidates and record-breaking single-molecule magnets.[29,38,46,47] Arene ligands provide an intriguing avenue towards engineering the electronic structure of rare earth and actinide ions due to their ability to act as donors into (vacant) *d*-orbitals, and also to accept back donation from electron-rich metals (**Figure 1**), stabilising lower oxidation states.[48-53] Indeed, the only examples of formally zero-valent rare earth complexes are within $[M(\eta^6\text{-}C_6R_6)_2]$ frameworks, and some have thermodynamic stabilities which approach or surpass that of transition metal analogues.[54-58]

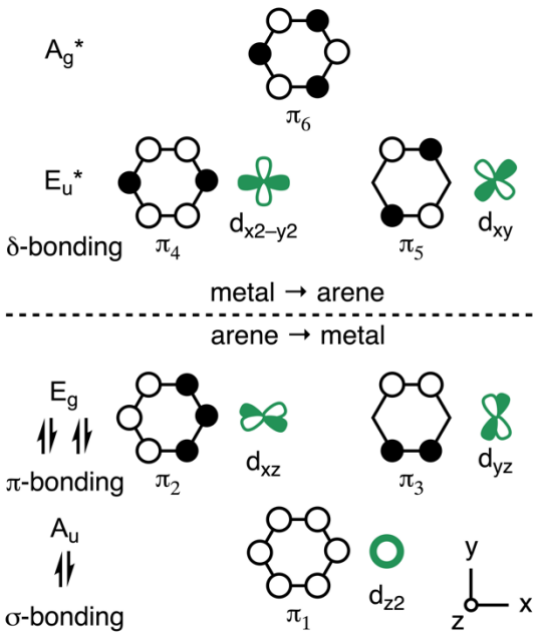

Figure 1. An illustration of metal-arene symmetry allowed orbital interactions for a d^0 metal, showing the divide between arene → metal, and metal→ arene donation.

Herein we present a series of structurally analogous formally divalent rare-earth complexes of the form [M(NHAr$^{i\text{Pr6}}$)$_2$] (M = Sc, Y, La, Sm, Eu, Tm, Yb; NHAr$^{i\text{Pr6}}$ = {N(H)C$_6$H$_3$-2,6-(C$_6$H$_2$-2,4,6-*i*Pr$_3$)$_2$}); we note that [Y(NHAr$^{i\text{Pr6}}$)$_2$] has been reported recently,[59] along with the U analogue in 2018.[60] All seven rare earth complexes contain close metal–arene contacts, however, only with Sc(II), Y(II), and La(II) do quantum chemical calculations reveal significant delocalization of a metal *d*-electron into ligand π-orbitals to form δ-bonding interactions, while the Sm(II), Eu(II), Tm(II) and Yb(II) complexes adopt non-bonding 4*f*$^{n+1}$ configurations. EPR and UV-Vis-NIR spectroscopies alongside density functional and *ab initio* calculations suggest a significant degree of metal and metal-bound arene character in the SOMO of the Sc, Y, and La complexes, as opposed to arene-radical character, and therefore support a formal oxidation state of M(II). These complexes represent a rare structurally analogous divalent rare earth series extending from the group 3 metals into the lanthanide series, and reveal the influence of arene coordination on the stability and accessibility of valence *d*-electrons with these elements.

Results and Discussion

Synthesis

Synthesis of the title complexes, [M(NHAr^{iPr6})$_2$] (**2M**, M = Sc, Y, La, Sm, Eu, Tm, Yb) proceeded *via* one of two routes (**Scheme 1**) dependent upon whether divalent halide precursors exist, or not.

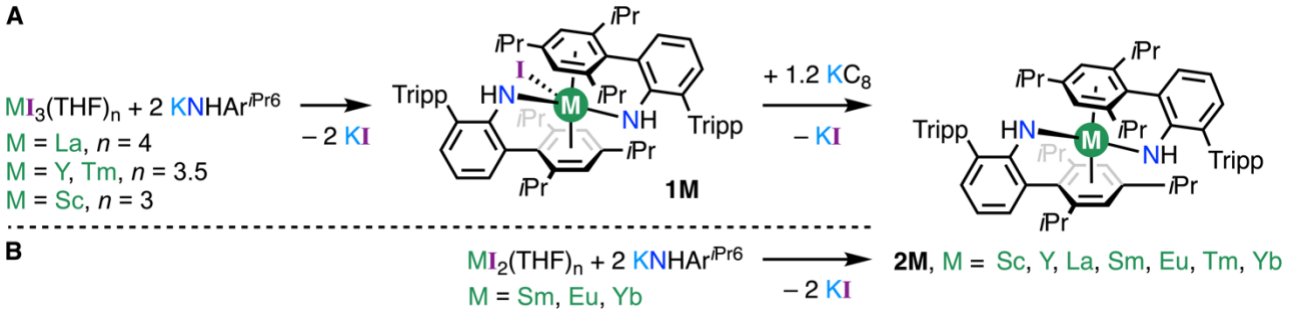

Scheme 1. Synthesis of (Route A) [M(NHAr^{iPr6})$_2$(I)] (**1M**, M = Sc, Y, La, Tm), and (Route B) [M(NHAr^{iPr6})$_2$] (M = Sc, Y, La, Sm, Eu, Tm, Yb). Tripp = {C$_6$H$_2$-2,4,6-*i*Pr$_3$}.

A reductive route was pursued (A in **Scheme 1**) for complexes with Sc, Y, La, and Tm, a beginning with trivalent [M(NHAr^{iPr6})$_2$(I)] (**1M**, M = Sc, Y, La, Tm). Complexes **1M** were synthesized from KNHAr^{iPr6} (refs. [61,62]) and the relevant rare earth tri-iodide salt MI$_3$(THF)$_n$ (*n* = 4, M = La; *n* = 3.5, M = Y, Tm; *n* = 3, M = Sc)[63] in Et$_2$O as bright yellow blocks in fair to good crystalline yields (47–62%). ^{1}H NMR spectroscopy of **1Sc**, **1Y**, and **1La** show that in solution the M···C$_{6\text{-arene}}$ interaction is dynamic as only three CH$_3$-*i*Pr doublets are seen, and the 2,6-*i*Pr groups show an "in" and "out" CH$_3$ resonance, while the 4-*i*Pr group freely rotates, affording a 12:12:12 d:d:d pattern (see *Supporting Information* for more detailed assignments). In the case of **1Y**, we were able to determine the ^{89}Y chemical shift (516 ppm), which couples to the anilido proton ($^2J_{HY}$ = <1 Hz) and is in excellent agreement with the prior report.[59]

Complexes [M(NHAr$^{i\text{Pr6}}$)$_2$] (**2M**, M = Sc, Y, La, Tm) were synthesized by reduction (KC_8, 1.2 equiv.) of the relevant trivalent **1M** precursor complex in Et_2O. Reaction mixtures immediately formed intense dark red/brown. Workup and crystallization from Et_2O at –30 °C gave poor to fair yields (25–43%) of dark crystals of **2Y** (red/green), **2La** (red/brown), and **2Tm** (red/brown). In the case of **2Sc**, dark red crystals of **2Sc** were grown from *n*-hexane at –30°C in 26% yield. For **2M** (M = Sm, Eu, Yb), salt elimination using KNHAr$^{i\text{Pr6}}$ and divalent iodide precursors $MI_2(THF)_2$ (M = Sm, Eu, Yb)[64] gave poor to excellent crystalline yields (20%, **2Eu**; to 82%, **2Yb**). Higher yields can be obtained by crystallization from *n*-hexane rather than Et_2O; though, on occasion, the resultant crystal structures feature extensive whole-ligand disorder. The colours of **2Eu** (bright orange) and **2Sm** (dark green) are typical for divalent complexes with these metals, while **2Yb** was isolated as dark blue/green planks. To provide data points for comparison with **2Sm** and **2Yb**, we attempted to synthesize trivalent **1Sm** and **1Yb** by salt elimination reactions between $MI_3(THF)_n$ (M = Sm, Yb) and two equivalents of KNHAr$^{i\text{Pr6}}$. Traces of teal green **1Yb** were isolated as part of an impure mixture along with **3**, (HN=C_6H_3-2,6-(2,4,6-*i*Pr_3)-4-{HN-C_6H_3-2,6-(2,4,6-*i*Pr_3)$_2$) (**Scheme 2**), which appears to be the product of head-to-tail radical coupling of two equivalents of {NHAr$^{i\text{Pr6}}$}$^{\cdot}$, and has been seen previously (see *Supporting Information*, and **Scheme 2**).[65] Complex **1Sm** could not be isolated by this methodology, impure or otherwise, and no attempt was made to synthesize **1Eu**. We were unable to identify any M(II) products formed as part of the presumed radical process.

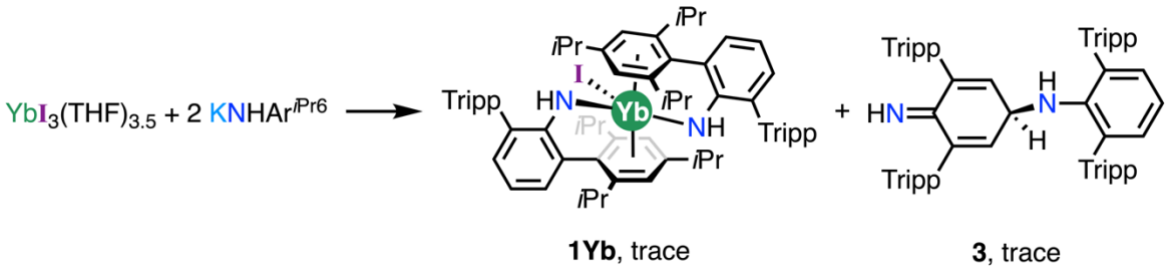

Scheme 2. Attempted synthesis of [Yb(NHAr^{iPr6})$_2$(I)], and isolation of **3**, (HN=C$_6$H$_3$-2,6-(2,4,6-*i*Pr$_3$)-4-{HN-C$_6$H$_3$-2,6-(2,4,6-*i*Pr$_3$)$_2$).

Unlike the spectra of **1Sc**, **1Y**, and **1La**, which showed both metal-bound and "terminal" Tripp groups to be in exchange, the ^{1}H NMR spectrum of diamagnetic **2Yb** shows six doublets for the CH$_3$-*i*Pr groups, along with a single N(H) resonance; thus, **2Yb** is C_2 symmetric in solution, and the metal-bound and "terminal" Tripp groups do not appreciably exchange at room temperature. A variable temperature ^{1}H NMR study in toluene-d_8 shows the CH$_3$-*i*Pr peaks begin to coalesce just above room temperature, at 308 K, but that full equilibrium is not reached until *ca*. 358 K (**Figures S40** and **S41**). The ^{171}Yb NMR spectrum gave a single peak at –83 ppm, and the ^{1}H–^{171}Yb HMBC revealed coupling to the anilido proton, and also to 3,5-CH groups on the Tripp ring. See the *Supporting Information* for NMR spectra of all complexes.

Molecular structures

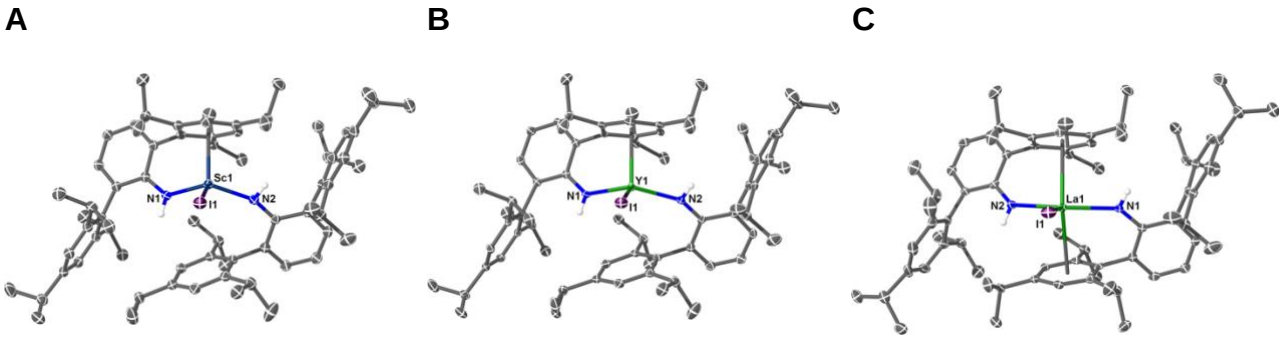

Figure 2. Molecular structures: (A) [Sc(NHAr$^{i\text{Pr6}}$)$_2$(I)] (**1Sc**); (B) [Y(NHAr$^{i\text{Pr6}}$)$_2$(I)] (**1Y**); (C) [La(NHAr$^{i\text{Pr6}}$)$_2$(I)] (**1La**). Thermal ellipsoids have been set at 40% probability. H-atoms except those on N–H groups, solvents of crystallization, and disordered components have been removed for clarity.

Single crystal X-ray diffraction studies on trivalent **1M** (M = Sc, Y, La) complexes reveal that all are *pseudo* three-coordinate (neglecting the bound arene), all crystallizing in the triclinic space group $\bar{P}1$ (Z' = 1) along with two toluene molecules of crystallization per formula unit. The structures of **1Sc**, **1Y**, and **1La** are shown in **Figure 2** (panels A–C). The trend of M–N bond lengths (**1Sc**: 2.0643(15) and 2.0909(15) Å; **1Y**: 2.2167(17) and 2.2452(17) Å; **1La**: 2.399(2) and 2.402(2) Å) reflects the relative differences in the ionic radii of these metals (six-coordinate Sc(III) = 0.745 Å; Y(III) = 0.900 Å; La(III) = 1.035 Å).[66] While the two M–N bond lengths in **1La** are statistically indistinguishable, in both **1Sc** and **1Y** one is shorter than the other by a significant amount (Δ_{M-N} in **1Sc** = 0.0266(15) Å; and in **1Y** = 0.0285(17) Å where the number in parenthesis is the root sum of squares of their respective standard uncertainties). This reflects the different M···C$_{6\text{-arene}}$ contacts present in **1Sc**, and **1Y**, versus those in **1La**. In **1La**, the metal is sandwiched almost equally between two flanking {C$_6$H$_2$-2,4,6-*i*Pr$_3$} (Tripp) groups (La···C$_{6\text{-centroid}}$ = 2.8714(12)–2.8783(12) Å) – one from each of the two {NHAr$^{i\text{Pr6}}$} ligands, and so is trigonal planar about the heteroatoms (La···N$_2$I plane deviation = 0.0042(15) Å; Σ angles about La = 360.0(1)°). Conversely, **1Sc** and **1Y** only have

a single Tripp group close to the metal (M···$C_{6\text{-centroid}}$: **1Sc**, 2.3391(8) Å; and **1Y**, 2.4949(9) Å). The structure of **1Y** is comparable to that of the recently reported chloride congener, [Y(NHAr$^{i\text{Pr6}}$)$_2$(Cl)],[59] where the Y···$C_{6\text{-centroid}}$ (2.4952(14) Å), Y–N (2.213(2)–2.249(2) Å), and N–Y–N (133.75(10)°) metrics either overlap within the 3σ criterion to those of **1Y**, or are very close. This suggests the iodide and chloride ligands do not impart any significant stereochemical effects on the structure of these complexes. See the *Supporting Information* for the structures of **1Tm** and **1Yb**, along with **Table S8**, for a comparison of **1M** complexes.

Formally divalent **2M** (M = Sc, Y, La, Sm, Eu, Tm, Yb) all bear the same general connectivity, but there are key differences. Complex **2Sc** crystallizes in the triclinic space group $\bar{P}1$ (*Z*' = 1), while **2La** crystallizes in the monoclinic space group $P2_1/c$ (*Z*' = 1), and **2Y** in $C2/c$ (*Z*' = 0.5) – the other half of **2Y** is generated by a 2-fold rotation about the crystallographic *b* vector. The other Ln(II) complexes all crystallize with *Z*' = 1 in monoclinic space groups (in brackets) – **2Sm** ($P2_1/n$), **2Eu** ($C2$), **2Yb** ($C2$), **2Tm** ($P2_1/c$). **Figure 3** shows the molecular structures of **2Sc**, **2Y**, and **2La** (see *Supporting Information* for **2Sm**, **2Eu**, **2Tm**, and **2Yb**).

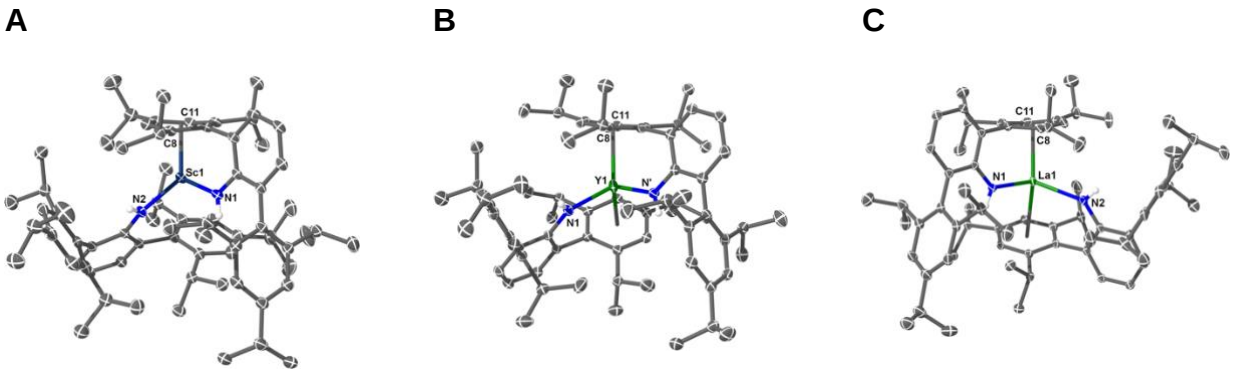

Figure 3. Molecular structures: (A) [Sc(NHAr$^{i\text{Pr6}}$)$_2$] (**2Sc**); (B) [Y(NHAr$^{i\text{Pr6}}$)$_2$] (**2Y**); (C) [La(NHAr$^{i\text{Pr6}}$)$_2$] (**2La**). Thermal ellipsoids have been set at 40% probability. H-atoms except those on N–H groups, solvents of crystallization, and disordered components have been removed for clarity.

All **2M** complexes show two flanking Tripp groups (one from each {NHAr$^{i\text{Pr}6}$} ligand) oriented towards the metal. When viewed along the $C_{6\text{-centroid}}\cdots C_{6\text{-centroid}}$ axis, these two Tripp groups are either fully eclipsed due to the crystallographic C_2 symmetry (**2Y**, **2Eu**, and **2Yb**), or are *pseudo*-eclipsed (**2Sc**, **2La**, **2Sm**, and **2Tm**) – see **Figure 4** for an illustration. The most salient feature of these complexes is the nature of the arene ring(s) which have close metal contacts as it provides insight into the electronic structure *vis-à-vis* metal- or ligand-centred reduction.[67,68] In the following sections, we shall continue to use the term "$C_{6\text{-centroid}}$" to refer to the calculated centroid of ligand Tripp groups, though in the case of **2Sc**, **2Y**, **2La** (and previously reported **2U**),[59,60] it is not strictly appropriate to define a centroid as the rings are non-planar (*vide infra*).

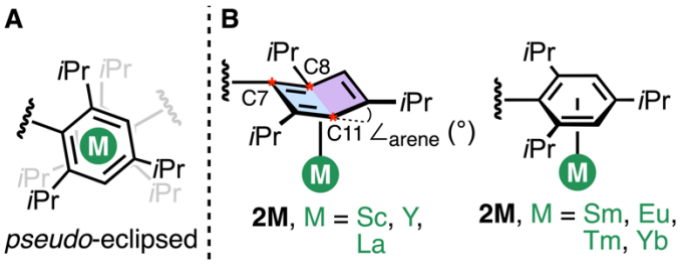

Figure 4. (A) Top-down illustration of the (Tripp)···M···(Tripp) unit in the **2M** complexes, highlighting ring carbon atoms C7, C8, and C11; (B) an illustration of the ring distortion in **2Sc**, **2Y**, and **2La**, *vs* that of **2Sm**, **2Eu**, **2Tm**, and **2Yb** – blue and pink panels, and red stars, are to guide the eye, and $\angle_{\text{arene}}$ (°) is the angle which subtends the two C_4-planes which lay either side of a line defined by C8 and C11.

Both **2Sc** and **2La** have one Tripp group closely approaching the metal, which is no longer planar, instead showing an "open book" deformation which hinges on two *para*-disposed C-atoms [see **Figure 4**; atoms C(8) and C(11)]. A "hinge angle" ($\angle_{\text{arene}}$) can be calculated by defining two separate C_4-planes which hinge upon C(8) and C(11). $\angle_{\text{arene}}$ is 11.43(11)° for **2Sc**, and 12.9(3)° for **2La**. In **2Sc**, the next shortest $M\cdots C_{6\text{-centroid}}$ distance to a Tripp group

(3.8304(7) Å) is too far away to constitute a strong interaction; however, in **2La** the equivalent group is only *ca*. 0.4 Å further (M···$C_{6\text{-centroid}}$ = 2.8348(12) Å) than the deformed arene ring, but it is planar to within the precision of the measurement. The structure of **2Sc** is similar to that of the Ti(IV) analogue **2Ti**,[68] but the latter exhibits a $\angle_{arene}$ of 24.19(18)° and is diamagnetic by SQUID magnetometry, indicating the presence of a dianionic Tripp ring. The M–C distances in **2La** compare reasonably well to those in previously reported **2U** given their similar ionic radii (six-coordinate La(III) = 1.032 Å, U(III) = 1.025 Å) in **2U** (2.731(3) Å and 2.723(3) Å), after accounting for common differences in Ln–E *vs* An–E bond lengths. In **2U**,[60] $\angle_{arene}$ is 9.5(1)° – though note in this complex one of the ligands is generated by crystallographic C_2 symmetry, and so it bears two close M···$C_{6\text{-arene}}$ interactions, both of which show deformation of the Tripp groups. The structure of **2Y** is equivalent to that previously reported,[59] despite the presence of different lattice solvents (Et_2O here, THF previously). Like **2U**,[60] complex **2Y** has C_2 symmetry with only one crystallographically-unique ligand, and this has an "open-book" arene deformation ($\angle_{arene}$ = 7.27(12)°).[59] There is no clear trend in $\angle_{arene}$ (**2Y** < **2U** < **2La** < **2Sc**) except that both C_2 symmetric complexes (**2Y** and **2U**) have smaller $\angle_{arene}$ angles,[59,60] and that larger values correlate with a greater degree of metal electron localisation by EPR spectroscopy and DFT calculations (*vide infra*), though **2Ti** clearly places an upper limit on this trend.[68] It is noteworthy that the previously reported neutral formal Gd(0) complex, [Gd(C_6H_3-1,3,5-*t*Bu)$_2$], also displays two symmetry-equivalent slightly distorted arene rings ($\angle_{arene}$ = 3.1(3)°).[54] The structures for the remaining divalent complexes, **2Sm**, **2Eu**, **2Tm**, and **2Yb**, are largely analogous to that of **2La**, with the exception only **2La** shows signs of arene deformation in Tripp groups which have close contacts with the metal, and so the former four help to contextualise the arene deformations seen in **2Sc**, **2Y**,[59] **2La**, and **2U**.[60] **Table 1** summarizes structural parameters for all **2M** complexes (M = Sc, Y, La, Sm, Eu, Tm, Yb, U) now reported.[59,60]

Table 1. Bond lengths (Å) and angles (°) for [M(NHAr^{i}^{Pr6})$_2$] (**2M**, M = Sc, Y, La, Sm, Eu, Tm, Yb, U).[59,60]

(Å or °)		2Sc	2Y [A]	2La	2Sm	2Eu [B]	2Tm	2Yb [B]	2U [C]
M–N	N(1)	2.0884(11)	2.2600(12)	2.395(3)	2.412(2)	2.411(4) 2.414(5) [B]	2.3060(17)	2.310(6) 2.294(6) [B]	2.330(2)
	N(2)	2.0678(10)	– [A]	2.434(3)	2.425(2)	– [B]	2.3169(18)	– [B]	– [A]
M–C$_{6\text{-range}}$	Ring(1)	2.3913(12)– 2.6304(14)	2.7276(14)– 2.9273(15)	2.778(16)– 2.971(9)	2.955(3)– 3.160(3)	2.972(4)– 3.176(5)	2.8015(19)– 2.971(2)	2.840(6)– 3.047(6)	2.723(3)– 2.870(3)
	Ring(2)	–	– [A]	3.047(3)– 3.240(3)	2.953(3)– 3.201(3)	– [B]	2.819(2)–3.118(2)	– [B]	– [A]
M–C	C(8)	2.3913(12)	2.7684(14)	2.843(13)	–	–	–	–	2.731(3)
	C(11)	2.5418(13)	2.7859(15)	2.903(12)	–	–	–	–	2.723(3)
Arene fold angle		11.43(11)	7.27(12)	12.9(9)	–	–	–	–	9.3(2)

[A] The solid-state structure is C_2-symmetric so there is a single metal and ligand per asymmetric unit; [B] The solid-state structures show two half-molecules in the asymmetric unit, so M(1) and M(2) each have only one unique ligand; [C] Note that the atom numbering in previously reported **2U** differs from that used here (C8 and C11 here are C12 and C9 respectively in the prior report).[60]

UV-Vis-NIR spectroscopy

UV-Vis-NIR spectra were collected for **1M** (M = Sc, Y, La, Tm) and **2M** (M = Sc, Y, La, Sm, Eu, Yb) at ambient temperature as 1 mM solutions in Et_2O. **Figure 5** shows a comparison between **1M** and **2M** for Sc, Y, and La, and also **2Sm**, **2Eu**, **2Tm**, and **2Yb** (see **Figures S57** to **S68** for individual spectra).

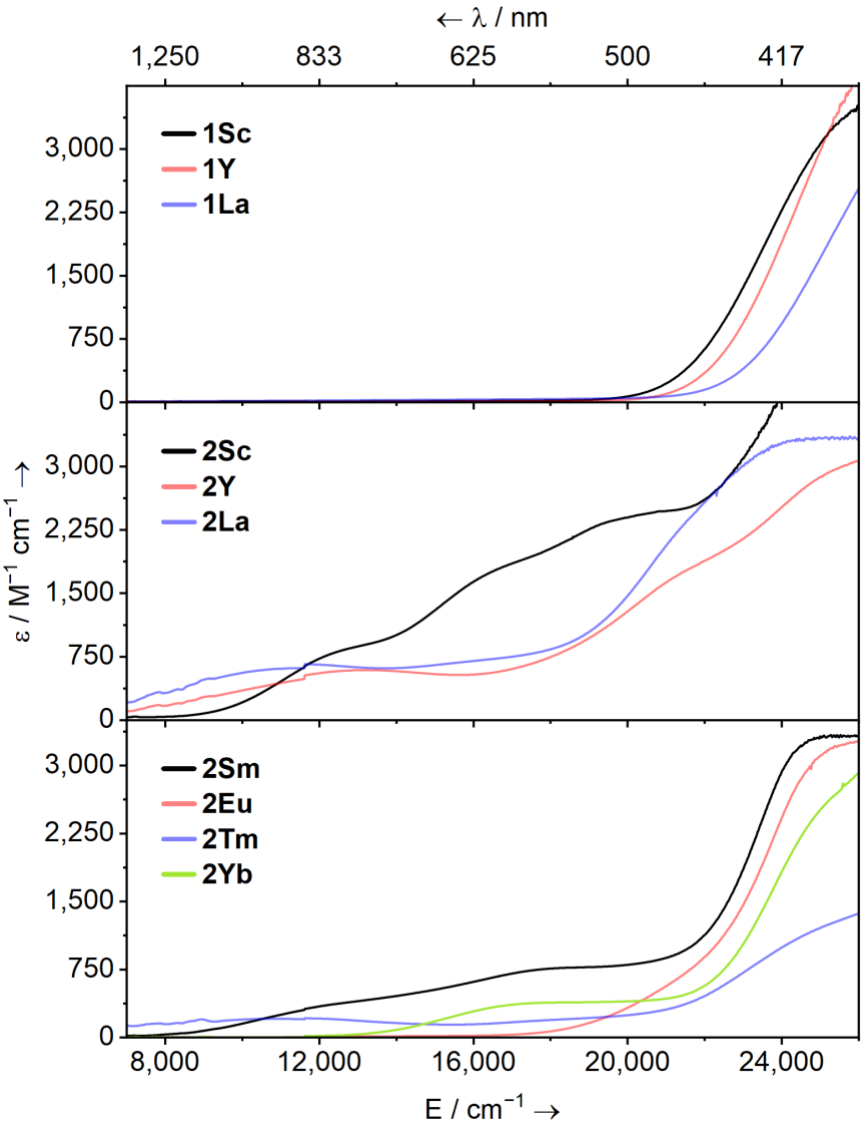

Figure 5. Solution UV-Vis-NIR spectra of [M(NHAr^{iPr6})(I)] (**1M**, M = Sc, Y, La; top) and [M(NHAr^{iPr6})] (**2M**, middle, M = Sc, Y, La; bottom, M = Sm, Eu, Tm, Yb) – all as 1 mM solutions in Et_2O and shown between 7,000–26,000 cm^{-1} (1,429–385 nm) at ambient temperature.

The UV-Vis-NIR spectra of **1Sc**, **1Y**, and **1La** are largely uninformative and show only a broad ligand-to-metal charge transfer (LMCT) process which tails from *ca*. 20,000 cm^{-1} (500 nm) to well into the UV region, accounting for the intense yellow colour of all three complexes in solution. The spectrum of **2Sc** is richly featured and shows three well-resolved absorptions at 13,412 cm^{-1} (756 nm, 805 M^{-1} cm^{-1}), 17,394 cm^{-1} (575 nm, 1,727 M^{-1} cm^{-1}), and 21,315 cm^{-1} (469 nm, 2,471 M^{-1} cm^{-1}). The modest intensity of these peaks coupled with their energies suggests 3*d*→3*d* transitions and/or metal-to-ligand charge transfer (MLCT) bands. For **2Y** we can resolve two peaks at 13,709 cm^{-1} (729 nm, 594 M^{-1} cm^{-1}) and 21,589 (463 nm, 1,787 M^{-1} cm^{-1}), while a third is visible tailing in from above 26,000 cm^{-1} (385 nm); the latter was previously reported at 33,670 cm^{-1} (297 nm, 1,040 M^{-1} cm^{-1}).[59] In that report, the transitions were suggested to be charge transfer processes. However, we suggest some may, in fact, be 4*d*→4*d* transitions on the basis of quantum chemical calculations (*vide infra*). Finally, in **2La**, a single clear peak is resolved at 12,253 cm^{-1} (816 nm, 650 M^{-1} cm^{-1}), with a second tentative peak around 24,000 cm^{-1} (417 nm). As for **2Sc**, and **2Y**, we suggest that the lowest energy peak in **2La** is a 5*d*→5*d* transition.

The UV-Vis-NIR spectra for trivalent **1Tm** (**Figure S60**) and **2Sm**, **2Eu**, **2Tm**, and **2Yb** as 1mM solutions in Et_2O (**Figure 5**, and **Figures S65** to **S68**) are typical for these elements in their respective oxidation states.[31,33,69-72] Complex **1Tm** shows a broad feature which tails from *ca*. 18,000 cm^{-1} (556 nm) into the UV region, and two distinctive sharp peaks at 12,723 cm^{-1} (786 nm, 44 M^{-1} cm^{-1}) and 14,556 cm^{-1} (687 nm, 51 M^{-1} cm^{-1}) for the $^3H_6 \rightarrow {}^3F_4$ and $^3H_6 \rightarrow {}^3F_{2/3}$ transitions, respectively. UV-Vis-NIR spectra of Sm(II), Tm(II), and Yb(II) often show moderately intense 4*f*→5*d* transitions, much like that of Ce(III), and indeed we see such features for **2Sm** at 12,337 cm^{-1} (811 nm, 364 M^{-1} cm^{-1}) and 18,784 cm^{-1} (532 nm, 774 M^{-1} cm^{-1}); for **2Tm** at 25,882 cm^{-1} (386 nm, 1,305 M^{-1} cm^{-1}) and 11,224 cm^{-1} (891 nm,

207 M^{-1} cm^{-1}); and for **2Yb** at 18,643 cm^{-1} (536 nm, 387 M^{-1} cm^{-1}). Complex **2Eu** displays no features within the UV-Vis-NIR spectral range except a broad LMCT which tails from 16,000 cm^{-1} (625 nm) into the UV region, as is typical for $^8S_{7/2}$ ions.[73]

SQUID magnetometry

For lanthanide ions with $4f^n$ or $4f^{n+1}$ valence electron configurations, the ground state is usually well described using the Russell-Saunders or *L-S* coupling scheme ($^{2S+1}L_J$), as interelectronic repulsion is much larger than spin-orbit coupling (SOC), which in turn is much larger than ligand field effects. The ground state is, therefore, usually well-isolated and diagnostic for a given 4*f* electron count. Direct current (DC) magnetic susceptibility data were collected for **1Tm**, and **2M** (M = Sc, Y, La, Sm, Eu, Tm) from 1.8 to 300 K under an applied field of 1 kOe (**Figure S83** to **S93**). At 300 K, the $\chi_M T$ (χ_M is the molar magnetic susceptibility) values for **1Tm** (6.69 cm^3 mol^{-1} K), **2Eu** (7.27 cm^3 mol^{-1} K), and **2Tm** (2.47 cm^3 mol^{-1} K) closely match the theoretical values for $4f^{n+1}$ configurations (Tm(III), $4f^{12}$, $^3H_6$, 7.15 cm^3 mol^{-1}; Eu(II), $4f^7$, $^8S_{7/2}$, 7.88 cm^3 mol^{-1} K; Tm(II), $4f^{13}$, $^2F_{7/2}$, 2.57 cm^3 mol^{-1} K). For **2Sm** ($4f^6$) the value at 300 K is 1.43 cm^3 mol^{-1} K, which in the range observed for Eu(III) ($4f^6$) complexes (1.3 to 1.5 cm^3 mol^{-1} K),[74] and which is non-zero despite a $^7F_0$ ground state due to population of excited ^7F_J states.[69-71] For comparison, $\chi_M T$ for **2Sm** would be expected to be < 0.7 cm^3 mol^{-1} K based on the *L-S* or *J-s* schemes with a $4f^5 5d^1$ configuration. $\chi_M T$ for **2Sm** decreases slowly from 300 K to 100 K, then more rapidly down to a value of 0.02 cm^3 mol^{-1} K at 1.8 K, which is consistent with a $^7F_0$ ground state, thus we assign **2Sm** as having a $4f^6$ configuration.

Complexes **2Sc**, **2Y** and **2La** exhibit $\chi_M T$ values at 300 K (0.31, 0.36, and 0.29 cm^3 mol^{-1} K respectively) which are in reasonable agreement with the spin-only value (0.375 m^3 mol^{-1}

K) expected for an $S = {}^1/_2$ system (0.375 m^3 mol^{-1} K for $g = 2.00$), and hence with a formal d^1 configuration. In each case, the moment is essentially temperature invariant across the entire range down to *ca*. 8–10 K, where a sudden drop can be seen, though this varies across independently synthesized samples (see *Supporting Information* for more details). Given the proximity of metal centres in these complexes (**2Sc** (9.976(2) Å), **2La** (10.1745(8) Å), and **2Y** (12.3175(2) Å) and the extensive spin density on the ligands (see below), it is likely that intermolecular interactions explain the low-temperature deviations.

Electronic structure calculations

Unrestricted Kohn-Sham density-functional theory (DFT) calculations were performed on **2Sc**, **2Y**, **2La**, **2Tm** ($S = {}^1/_2$), **2Sm** ($S = 3$), **2Eu** ($S = {}^7/_2$), and **2Yb** ($S = 0$) using partially geometry-optimized structures of all **2M** complexes to elucidate the ground-state electronic structures and excited-state properties (see *Supporting Information* for full details). No symmetry constraints were imposed.

Löwdin population analyses of the highest occupied molecular orbitals (HOMOs) for the traditional divalent complexes **2Sm**, **2Eu**, **2Yb**, and **2Tm** are entirely consistent with formulations containing essentially purely metal-localized 4*f* electrons (**Table S16**), and in agreement with experimental data. In all cases, the Löwdin spin population is also almost entirely 4*f*-based, and in agreement with expected values. The SOMOs of C_1 symmetric **2Sc** and **2La** have 36% 3*d* (with 4% 4*s*) and 14% 5*d* (with 10% 4*f* and 1% 6*s*) metal character respectively, with the bound $C_{6\text{-arene}}$ ring making up another 41% (**2Sc**) and 56% (**2La**) in each case. These SOMOs are dominated by *d*-orbitals engaging in δ-bonding interactions to the metal-bound Tripp group (**Figure 6** panels A and C); defining the M-bound Tripp direction as z, the d-orbital contribution is dominated by d_{x2-y2} (mixing in small quantities of d_{z2} in this axis system can make this superficially resemble d_{x2} or d_{y2}). In the case of **2Y**

(**Figure 6** panel B) which has crystallographic C_2 symmetry, the SOMO is extensively delocalized across both of the (equivalent) metal-bound Tripp groups such that the SOMO composition is only 14% Y (12% 4*d*, 0.5% 5*s*), while the $C_{6\text{-arene}}$ rings comprise another 64.6% combined – the SOMO resembles a severely delocalized δ-bonding interaction at arbitrarily large isovalues, but when compared to **2Sc** and **2La** there is little similarity. These results agree well with previous work on **2Y**.[59] Still, clearly, it is an outlier in having two deformed Tripp groups and a significantly more delocalized SOMO than **2Sc** and **2La**. However, this may simply be an artefact of using the solid-state structure as a starting point for these calculations (*vide infra*).

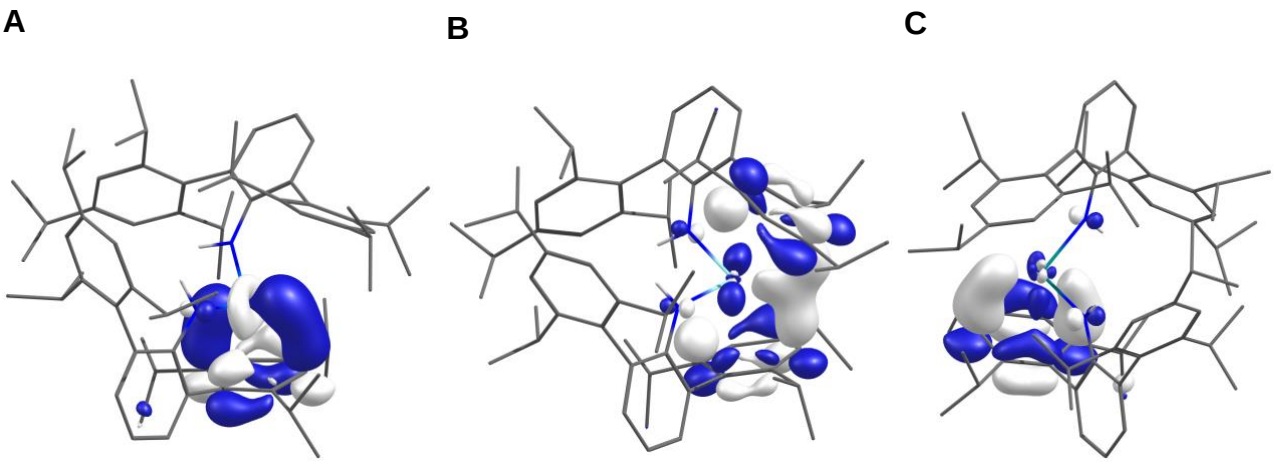

Figure 6. SOMOs of **2Sc** (A), **2Y** (B), and **2La** (C) with an isovalue = 0.05, using the geometry derived from single crystal X-ray diffraction with H-atoms optimized (**2Sc**, **2Y**), or with select disordered C-atoms and all H-atoms optimized (**2La**). H-atoms except those of the N(H) group omitted for clarity.

To determine the nature of the electronic excitations in these complexes, time-dependent DFT (TD-DFT) and simplified TD-DFT (sTD-DFT) calculations have been performed across a range of functionals to model the UV-Vis-NIR spectra of **2Sc**, **2Y**, and **2La**. The conductor-like continuum polarization model (C-PCM) was employed throughout, and see the *Supporting Information* (**Figures S101** to **S106**) for a comparison of the TD-DFT and sTD-DFT methods, and all functionals examined.[75,76] For comparative purposes, **Figure 7** shows

the results for all three complexes using the TPSSh functional which enables comparison to previous works.[20,29,30,42,77-79]

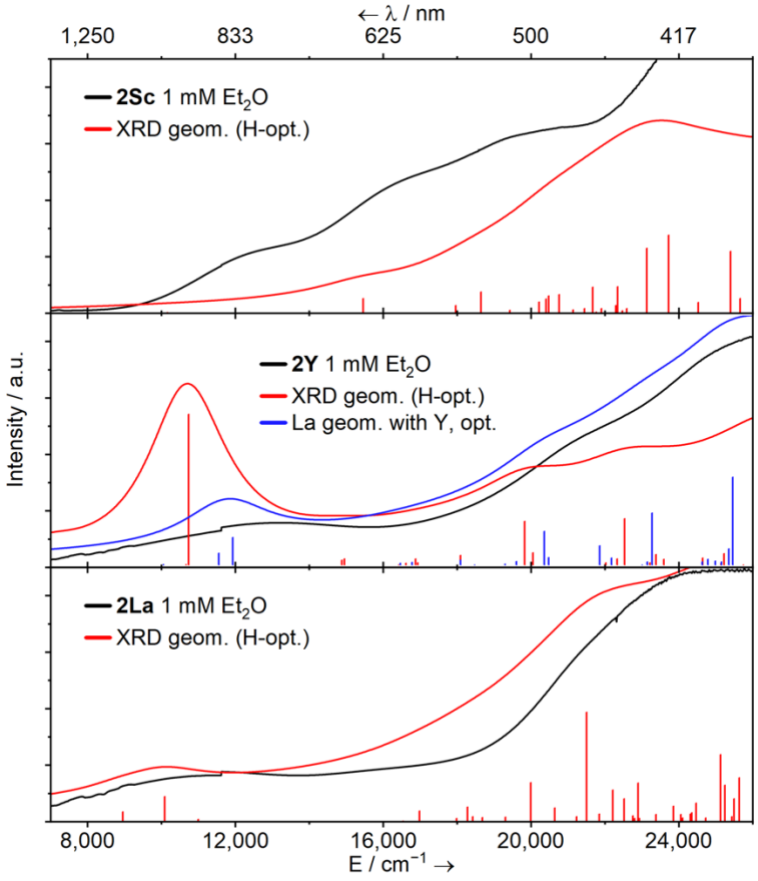

Figure 7. Experimental (1 mM, Et_2O, black), calculated sTD-DFT transitions (red and blue vertical lines), and simulated spectra (red and blue solid lines, with Gaussian broadening and a linewidth factor of $25 \times \sqrt{E}$) UV-Vis-NIR spectra for complexes **2Sc**, **2Y** (and **2Y-Et₂O**) and **2La** Calculated transitions were performed using a solvent model accounting for the dielectric constant (ε) and refractive index (n_D) of Et_2O.

The features of **2Sc** and **La** are reasonably well represented in the DFT-calculated transitions and simulated spectra. The intensity of the lowest energy transition in **2Sc** is under-predicted using the TPSSh/sTD-DFT approach but is recovered using TPSSh/TD-DFT or PBE/sTD-DFT. Inspection of the Natural Transition Orbitals (NTOs) from TD-DFT calculations (**Figure S108**) allows the assignment of the three broad features in the

experimental spectrum of **2Sc** as 3*d*→3*d* transitions, the lowest energy of which resembles a $3d_{(xy/x2-y2)}$→$3d_{(x2-y2/xy)}$ transition maintaining the δ-bonding interaction. For **2La**, the lowest energy feature arises from two transitions (see **Figure S110**), the dominant component of which resembles a $5d_{(xy/x2-y2)}$→$5d_{(x2-y2/xy)}$ excitation, while the next two lowest energy features resemble a combination of MLCT and 5*d*→5*d* transitions *i.e.* the La···$C_{6\text{-arene}}$ ($5d_{(xy/x2-y2)}$) δ-bond is excited into a new La···$C_{6\text{-arene}}$ ($5d_{(xy/x2-y2)}$) δ-bond to the opposite Tripp ring. However, we find poor agreement between the UV-Vis-NIR data and (s)TD-DFT calculations for **2Y** across all functionals and methodologies.

To better understand the optical spectra of **2Y**, we have explored the possibility that the C_2-symmetry present in the X-ray structure is an artefact of crystal packing effects and that the solution-state geometry may be different. The full structure of complex **2Y** was optimized in both the gas phase and Et_2O solvent starting from the lower-symmetry geometry of **2La**. Both optimized geometries retain structures with only one Tripp group deformed and tightly bound to the metal (*i.e.* like **2Sc** and **2La**), and are true local minima on the potential energy surface. We then performed TD-DFT and sTD-DFT calculations on the Et_2O solvent continuum geometry (**2Y-Et$_2$O**) using the same methodology as above (**Figure 7** middle panel, blue line). The substantial improvement in agreement between the experimental and calculated spectra suggests that the solution-state structure of **2Y** in Et_2O is more similar to the solid-state structures of **2Sc** and **2La**, than it is to its own crystal structure. Löwdin population analysis of the SOMO of **2Y-Et$_2$O** shows it to be significantly more localized on the metal (**Figure S113**; 20% 4*d*, 2% 5*s*, and 1% 4*f* – total 25.9%; *cf.* 14% using the C_2-symmetric structure), while the single deformed Tripp group of **2Y-Et$_2$O** contributes almost as much (54.4%) as the combined total of the two Tripp groups in the C_2-symmetric structure (67.1%); these differences are also reflected in the Löwdin spin populations at the metal where **2Y-Et$_2$O** has a value of 0.245, while **2Y** has only 0.142. The lowest energy features

in the experimental UV-Vis-NIR spectrum of **2Y-Et$_2$O** appears to be comprised of two components which are both combinations of MLCT and 4*d*→4*d* transitions. In both, an MLCT transition, Y···C$_{6\text{-arene}}$ (4*d*$_{(xy/x2\text{-}y2)}$) δ-bond → C$_{6\text{-arene}}$ to the opposite Tripp ring resembles a formal reduction of the ring, while the other is a 4*d*$_{(xy/x2\text{-}y2)}$→4*d*$_{(x2\text{-}y2/xy)}$ transition.

Complete active space self-consistent field (CASSCF) calculations (see *Supplementary Information* for details) on **2M** confirm the DFT and experimental results discussed hitherto: **2Sc**, **2Y** and **2La** exhibit n*d*^{1} ground states with significant orbital mixing with the arene ligand(s) (**Figures S120** to **S123**), and **2Sm**, **2Eu**, **2Tm** and **2Yb** have 4*f*$^{n+1}$ ground states. Calculations for the lowest-lying excitations in **2Sc**, **2Y** and **2La** including multi-configurational pair-density functional theory (MC-PDFT) corrections for dynamic correlation show n*d*/arene→n*d*/arene excitations in the UV-Vis-NIR range, in good agreement with the experimental spectra (**Figure S124**). The character of these excitations is broadly in line with that found using (s)TD-DFT, where the lowest-lying excitations for **2Sc** are mostly localized to one side of the molecule and resemble *d*→*d* transitions, while some for **2La** and **2Y-Et$_2$O** are combined MLCT and 5*d*→5*d* transitions to the opposite Tripp ring.

EPR spectroscopy

EPR spectroscopy was used to study the orbitally non-degenerate species **2Sc**, **2Y** and **2La**. All three are EPR active as polycrystalline solids and in solution (1 mM Et$_2$O or *n*Pr$_2$O); spectra of **2Y** in Et$_2$O have been reported previously. We find better resolved frozen solution spectra in *n*Pr$_2$O than in Et$_2$O (although the spectra are consistent; see *Supporting Information*), although for **2Sc** and **2La** we were able to obtain reliable fluid solution spectra to higher temperatures in Et$_2$O (*i.e.* the samples decomposed on thawing more rapidly in

nPr_2O, than in Et_2O). The latter is important because the greater spectral spread and hyperfine anisotropy for these complexes than for **2Y** means that higher temperatures are required for truly isotropic spectra to be obtained (*i.e.* for tumbling rates in solution being sufficient to average out anisotropy). For solution studies, spectra were measured of the samples in both *n*Pr_2O and Et_2O (melting points 151 K and 157 K, respectively).

X-band spectra of powders at room temperature are partially metal hyperfine-resolved for **2Sc** (^{45}Sc, I = 7/2, 100% abundant) and **2Y** (^{89}Y, I = 1/2, 100%) but unresolved for **2La** (^{139}La, I = 7/2, 100%) (see *Supporting Information*). For **2Sc**, a hyperfine octet is observed, with g = 2.000 and A = 145 MHz. For **2Y** we observe a hyperfine doublet (estimated A = 14 MHz) with $g_\perp$ = 2.005 and $g_\parallel$ = 1.995. For **2La**, we observe $g_\perp$ = 2.019 and $g_\parallel$ = 1.958. For **2Sc** and **2Y** there are changes in these parameters (smaller A and/or g-anisotropy) on cooling to 5 K, without any improvement in resolution. The limited resolution of the powder spectra is indicative of intermolecular interactions but also makes it difficult to discuss changes in electronic structure between solid and solution phases.

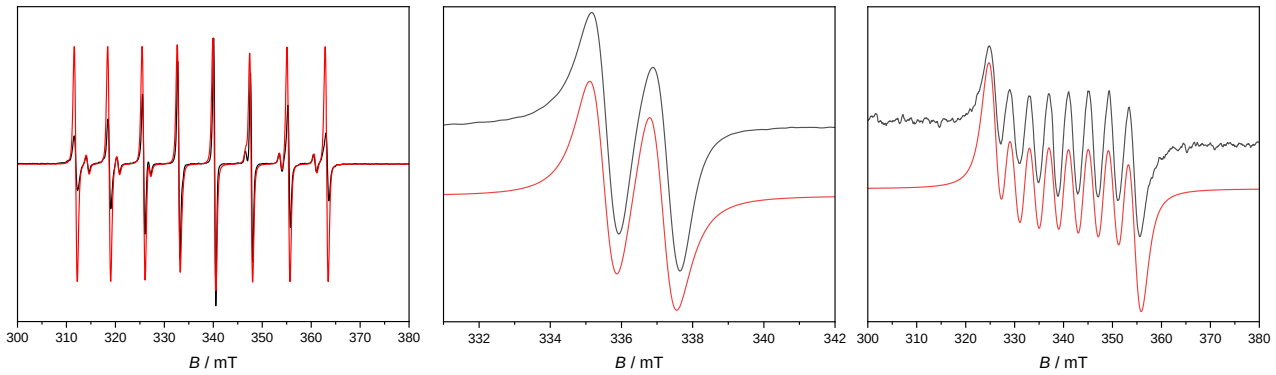

Figure 8. X-band cw EPR spectrum of 1 mM **2Sc** in Et_2O at 250 K (left), **2Y** in nPr_2O at 180 K (middle), and **2La** in Et_2O at 200 K (right). Black, experimental; red, simulations with parameters in the text.

Fluid solution spectra of **2Y** (180 K in *n*Pr_2O) and **2La** (220 K in Et_2O), see **Figure 8** middle and right panels respectively, give a well-resolved hyperfine doublet and octet, respectively,

due to hyperfine coupling of the unpaired electron to the metal nucleus consistent with the formal M(II) oxidation states. For **2Sc** (250 K in Et_2O, **Figure 8** left) we also obtain an octet, consistent with formal Sc(II), but there is a second and minor octet spectrum which differs subtly in the magnitude of the hyperfine. Hence, there are two formal Sc(II) species in solution, with a relative abundance of *ca*. 12:1 (we note that similar behaviour was observed recently in a different Sc(II) system reported by Evans).[79] The isotropic hyperfine couplings are A_{iso} = 205 MHz for **2Sc** (major species; minor species 186 MHz), 46 MHz for **2Y**, and 112 MHz for **2La**. In each case $g_{iso} < g_e$ (where g_e is the free electron *g*-value; g_{iso} = 1.9995, 1.998, 1.989, respectively), consistent with the formal d^1 configuration. The isotropic part of the hyperfine interaction derives from *s*-orbital spin density; from theoretical values of the hyperfine interaction for unit population of the valence *s*-orbitals (2823, −1250 and 6007 MHz for ^{45}Sc 4*s*, ^{89}Y 5*s* and ^{139}La 6*s*, respectively)[80] we estimate 7.3 (**2Sc**), 3.7 (**2Y**) and 2.0% (**2La**) *s*-orbital character of the SOMO. DFT calculations (see above) give 3.6, 1.8 and 1% valence *s*-orbital character (3.8, 2.0, 1.1% Löwdin spin populations), which are in good agreement with the experimental values, giving small percentages with the same trend. Experiment and calculations agree that **2Sc** has significantly the highest metal valence *s*-orbital spin density, then **2Y** > **2La**.

In frozen solutions at 60 K, well-resolved spectra are observed in each case (Figure 9). For **2Sc** we have been unable to obtain a satisfactory simulation of the spectrum assuming a single species, consistent with the fluid solution data (see *Supporting Information*). Despite the better resolution for **2Sc** in nPr$_2$O the spectrum recorded at 130 K in Et_2O gives a more satisfactory simulation. There is a dominant perpendicular component of the hyperfine of $A_\perp$ ≈ 210 MHz ($g_\perp$ = 2.002) which, taking A_{iso} = 205 from the dominant species in the fluid state, would give $A_\parallel$ = 195 MHz (assuming the same sign of $A_\perp$ and A_{iso}), and reasonable agreement is found with this value and $g_\parallel$ = 1.99. However, these parameters are not well

defined. For **2Y** and **2La** the spectra are axially symmetric within the resolution of the experiments. For **2Y** we find $g_{\perp}$ = 2.004, $g_{\parallel}$ = 1.986, with a near isotropic metal hyperfine of $A_{\perp}$ = 39, $A_{\parallel}$ = 36 MHz (we estimate an uncertainty of *ca*. 1 MHz). For **2La** we find $g_{\perp}$ = 2.005, $g_{\parallel}$ = 1.952 with $A_{\perp}$ = 110, $A_{\parallel}$ = 100 MHz (the latter parameters are defined by the features on the high-field edge of the spectrum). For both **2Y** and **2La**, the anisotropic hyperfines observed in frozen solution are close to those measured in fluid, hence $A_{\parallel}$, $A_{\perp}$ and A_{iso} all have the same sign. The subtle differences could imply a slight change in geometry on cooling.

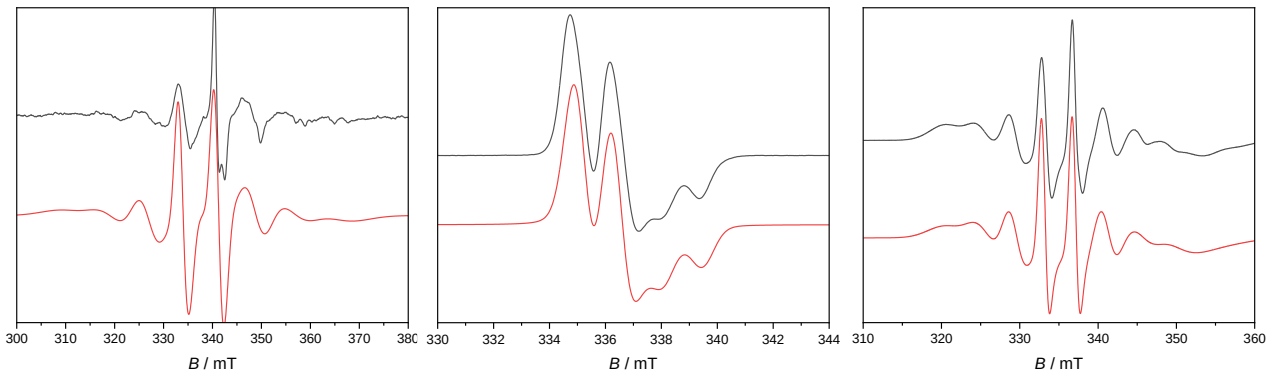

Figure 9. X–band cw EPR spectrum of 1mM **2Sc** (left) in Et_2O at 130 K, **2Y** (middle) and **2La** (right) in *n*Pr_2O at 60 K. Black experimental, red simulations.

The anisotropy of the *g*-values for **2Sc**, **2Y** and **2La** is due to the significant *d*-orbital character of the SOMO. The $g_{\perp} > g_{\parallel}$ pattern indicates a dominant $d_{x2\text{-}y2}$ contribution, while the greater deviation of $g_{\parallel}$ from g_e in the series **2La** > **2Y** > **2Sc** is in keeping with greater spin-orbit coupling for the heavier elements. A very crude analysis of the anisotropic metal hyperfine interaction to give the metal $d_{x2\text{-}y2}$ contribution to the SOMO [$A_{\parallel} - A_{\perp} = (-6/7)a^2P_d$, where *a* is the $d_{x2\text{-}y2}$ LCAO coefficient to the SOMO and P_d is the electron-nuclear dipolar coupling parameter] gives 7.3% for **2Sc** (P_d = 240 MHz for ^{45}Sc), 5.6% for **2Y** (P_d = −62.3 MHz for ^{89}Y) and 4.9% for **2La** (P_d = 237 MHz for ^{139}La). DFT calculations support the dominant $d_{x2\text{-}y2}$ metal-based contribution to the SOMO (where *z* is the M-bound arene

direction), but give much larger *d*-orbital contributions of 36, 20 and 14%, respectively (see above). Despite this, the calculations give reasonable agreement with the calculated hyperfine coupling constants (**Table 2**), implying an inadequacy in the crude analysis above. We have previously noted the discrepancy between the small anisotropic hyperfine components and calculated *d*-orbital spin density for related $[ML_3]^-$ systems.[38] The calculations approximate to axial symmetry with the "unique" axis (g_1, A_1 in **Table 2**) along the M-bound arene direction.

Table 2. Experimental (frozen solution) and calculated EPR parameters for **2Sc**, **2Y** and **2La**. Calculated hyperfine coupling constants in MHz; experimental A_{iso} taken from $(A_{\parallel} + 2A_{\perp})/3$. Calculated parameters for **2Y** are from **2Y-Et$_2$O**. The calculated g_1/A_1 axes are along the M-bound arene direction.

		g_1	g_2	g_3	A_1	A_2	A_3	A_{iso}
2Sc	**Exp.**	1.990	2.002		195	210		205
	Calc.	1.990	2.009	2.015	159	171	184	171
2Y	**Exp.**	1.986	2.004		36	39		38
(2Y-Et$_2$O)	**Calc.**	1.983	2.004	2.006	−47	−49	−50	−48
2La	**Exp.**	1.952	2.005		100	110		107
	Calc.	1.954	1.971	1.993	101	106	108	105

The DFT calculations give the SOMO as being dominated by the π_4 MO of the bound arene ring (as defined in **Figure 1**). The contribution of this arene to the SOMO is 41, 56 and 56% for **2Sc**, **2Y-Et$_2$O** and **2La**, respectively. The smallest contribution from this ligand orbital in **2Sc** correlates with the largest metal contributions. This π_4 MO has the correct symmetry to mix with the metal d_{x2-y2}, consistent with the EPR observations.

The EPR parameters, and electronic structure, of **2Sc**, **2Y** and **2La** are in contrast to related d^1 $[M^{II}L_3]^-$ species (M = Sc, Y, La, Lu; L = substituted Cp, aryloxide, amide) where the trigonal crystal field instead stabilises the d_{z2} orbital (*z* being defined by the three-fold axis) giving rise to characteristic $g_\perp < g_\parallel$ ($\approx g_e$) patterns.[29,38,81] The electronic structure in our materials has more in common with the $[Sc(Cp^{ttt})_2]$ sandwich compounds reported by Evans and co-workers,[79] where DFT calculations give a d_{x2-y2}-dominated metal contribution to the SOMO, and a similar $g_\perp > g_\parallel$ pattern can be observed from their (hyperfine unresolved) frozen solution EPR data. The hyperfine interactions in **2Sc**, **2Y** and **2La** are much smaller in magnitude than in the trigonal M(II) cyclopentadienyl-derived species; for example, $[Y(Cp^R)_3]^-$ with various substituents [$(Cp^R)_3$ = Cp'_3, Cp^t_3, $\{Cp''_2(C_5H_5)\}$] have $|A_{iso}|$ = 98–130 MHz;[38,82,83] and $[La(Cp'/Cp''/Cp^{tt})_3]^-$ have A_{iso} = 390–640 MHz.[38,81,84] As far as we are aware, the analogous $[Sc(C_5R_5)_3]^-$ have not been isolated. Hence, there is much greater metal character in the SOMOs of $[M(Cp^R)_3]^-$ than in **2M**. Comparing the asymmetric sandwich compounds **2M** with more symmetric sandwiches, $[Y(Cp^{iPr5})_2]$ and $[La(Cp^{iPr5})_2]$, which have A_{iso} = −505 and 2000 MHz, respectively,[31] and $[Sc(Cp^{ttt})_2]$ which has A_{iso} = 83 MHz,[79] seems curious as $[M(Cp^{iPr5})_2]$ (M = Y, La) have much larger A_{iso} than **2M**, while $[Sc(Cp^{ttt})_2]$ has much smaller A_{iso} than **2Sc**. However, such values can vary widely depending on the electron-donating ability of the Cp substituents; for example, Evans also reported spectra that are probably from $[Sc(Cp^*)_2]$ (not structurally confirmed) with A_{iso} = 824 MHz,[79] and $[La(Cp'')_3]^-$ and $[La(Cp^{tt})_3]^-$ have A_{iso} = 387 and 637 MHz, respectively.

Conclusion

A series of isostructural room-temperature stable divalent rare earth complexes supported by a *bis*-terphenyl anilide ligand framework, $[M(NHAr^{iPr6})_2]$ (**2M**; M = Sc, Y, La, Sm, Eu, Tm, Yb) has been reported which complements existing Y, U, and also Ti analogues.[59,60,68] All of these feature at least one (**2Sc**, **2Ti**) or two (all others) M···arene interaction(s). Within the

complexes studied herein, **2Sm**, **2Eu**, **2Tm**, and **2Yb**, possess essentially perfectly planar metal-bound arene groups, and SQUID magnetometry measurements unambiguously reveal these to be "traditional" divalent $4f^{n+1}$ complexes. This is in accord with the large $4f^{n+1} \rightarrow 4f^n5d^1$ promotional energies for these ions coupled with a lack of metal-to-ligand back-bonding.[39,40] DFT and CASSCF calculations further support this description. Meanwhile, formally divalent **2Sc**, **2Y**,[59] and **2La** show buckling of one (**2Sc** and **2La**) or both (**2Y**) bound arenes in the solid state, which is suggestive of charge accumulation in the arene ring. DFT and CASSCF calculations support conclusions drawn from the structural data that the bonding in these complexes is similar to that of transition metal arene complexes, whereby back-donation from the *d*-manifold of an electron-rich metal into π* orbitals of an arene ring produces δ-bonding interactions. This is in contrast to the previously reported titanium analogue, which features a diamagnetic closed shell Ti(IV) centre and an arene dianion.[68]

EPR and UV-Vis-NIR of the formal nd^1 **2Sc**, **2Y** and **2La** support a significantly delocalized SOMO over the metal valence n*d* and (n+1)*s* orbitals and the π_4 orbital of one bound arene ring. DFT and CASSCF calculations of *g*-tensors and hyperfine constants show excellent agreement with experimental data, which supports the validity of these theoretical models. Indeed, calculated electronic excitation energies for **2Sc** and **2La** align well with the UV-Vis-NIR solution absorption data, and allow the assignment of $d_{(xy/x2-y2)} \rightarrow d_{(xy/x2-y2)}$ and combined MLCT transitions. The solid-state structure of **2Y** is C_2-symmetric and features two buckled metal-bound arene rings; using this structure, calculated UV-Vis-NIR excitations and the solution-state EPR data have poor agreement, but good agreement is found with the solid-state EPR data. Optimisation of the structure of **2Y** based on the lower-symmetry **2La** structure to mimic a plausible solution-state structure with only a single buckled arene ring (**2Y-Et$_2$O**) predicts electronic excitation energies and EPR parameters in excellent agreement to the experimental solution UV-Vis-NIR and solution EPR data. This suggests

the metal environment in **2Y** changes dramatically between the solution and solid state, and that this can be observed spectroscopically.

By expanding the range of formally divalent rare earth ions within the [M(NHAr^{iPr6})$_2$] framework to include a large range of metal sizes and different formal valence electron configurations, there now exists an opportunity to probe the physicochemical properties of these species, which are sure to be both highly reactive and display complex physical properties. This, along with work to probe the limits of the *bis*-{NHAr^{iPr6}} framework to stabilise formally divalent *f*-block complexes, is ongoing.

Acknowledgements

We thank the Royal Society for a University Research Fellowship (URF\211271 to C.A.P.G, and URF\191320 to N.F.C.); and the UoM Department of Chemistry for the funding of a PhD studentship under EPSRC DTP (EP/W524347/1 to R.E.M, and EP/T517823/1 to T.H). We acknowledge funding from the EPSRC (EP/K039547/1, EP/V007580/1, EP/P001386/1, and EP/K039547/1 for NMR spectroscopy and X-ray diffraction). We also thank the EPSRC UK EPR National Research Facility including for access to the SQUID magnetometer (EP/W014521/1, EP/V035231/1, EPS033181/1). C.A.P.G and N.F.C. also thank the Computational Shared Facility at the University of Manchester for support. We thank Prof. Stephen Liddle for support (J.A.S). Elemental analyses were performed at the UoM by Mr Martin Jennings and Ms Anne Davies. We are also grateful to Profs. Aaron Odom and Selvan Demir for scientific discussions and encouragement.

Methodology

General considerations

KNHAr$^{i\text{Pr6}}$ was prepared from $H_2NAr^{i\text{Pr6}}$,[61] and BnK in toluene. Exemplar ^{1}H and $^{13}C\{^{1}H\}$ NMR spectra of KNHAr$^{i\text{Pr6}}$ are provided in **Figures S1** and **S2**. $[ScI_3(THF)_3]$ was synthesized in analogy to reported procedures for $[LaI_3(THF)_4]$ and $YI_3(THF)_{3.5}$.[63] Solution phase UV-Vis-NIR spectra were collected at ambient temperature using a PerkinElmer Lambda 1050 UV-Vis-NIR spectrometer. The solution was contained in a low volume (1 mL) screw-capped quartz cuvette (10 × 4 mm path length fluorescence cell). ATR FT-IR spectra of microcrystalline samples were collected using a Bruker ALPHA II FT-IR spectrometer equipped with a Platinum ATR module with diamond window. NMR spectroscopic data collection was performed on either a Bruker Avance III (400 MHz), Bruker Advance III HD (400 MHz), or Bruker Ascend (700 MHz) between 295 K to 299 K. Elemental microanalyses (C/H/N) were carried out by Martin Jennings and Anne Davies at the University of Manchester. SQUID magnetometry was conducted on finely ground samples immobilized in an eicosane matrix, and flame sealed in evacuated (10^{-3} mbar) 400 MHz Wilmad borosilicate NMR tubes. Static and variable-temperature magnetic moment data were recorded in an applied dc field of 0.1 T on a Quantum Design MPMS superconducting quantum interference device (SQUID) magnetometer. Care was taken to ensure the sample was at thermal equilibrium before each data point was measured, and samples were immobilized in an eicosane matrix to prevent sample reorientation during measurements. Diamagnetic corrections were applied using tabulated Pascal constants, and further corrected by measurement of a diamagnetic analogue complex, $[Ca(NHAr^{i\text{Pr6}})_2]\cdot(Et_2O)$ (**2Ca**)[1] in some instances. Measurements were also corrected for the effect of the blank sample holders (flame sealed Wilmad NMR tube and straw) and eicosane matrix. Cw EPR

[1] To be reported separately.

spectra were recorded using a Bruker EMX 300 EPR spectrometer operating at X-band frequency (*ca*. 9.8 GHz) and a Bruker EMX Micro EPR spectrometer operating at X-band frequency (*ca*. 9.4 GHz). Temperature variation and control were achieved using a Stinger closed-cycle helium gas cryostat (10–180 K) or the Bruker ER 4131VT-M liquid nitrogen cryostat (130–250 K). The samples were measured in quartz EPR tubes as polycrystalline solids or as 1 mM frozen solutions in Et_2O or nPr_2O (samples were flash frozen in liquid N_2 and then flame sealed under vacuum).

Synthesis

The synthesis of **1Sc** and **2Sc** is provided below as an example, all others were synthesized analogously. Please refer to the *Supporting Information* for more detail.

$[Sc(NHAr^{iPr6})_2(I)]\cdot(C_7H_8)_2$ (1Sc). Et_2O (50 mL) was added to a pre-cooled (–98°C) stirring mixture of solid $[ScI_3(THF)_3]$ (1.616 g, 2 mmol) and $KNHAr^{iPr6}$ (2.072 g, 4 mmol, 2 equiv.) in a glass Schlenk vessel equipped with a PTFE-coated stirrer bar. The mixture was allowed to warm to room temperature and quickly became yellow with a fine white precipitate, presumed to be KI. After stirring at room temperature overnight (16 hours), the volatiles were removed *in vacuo* (10^{-3} mbar) which left a bright yellow powder. Toluene (20 mL) was added and briefly (< 1 min) refluxed with manual agitation to loosen solids from the vessel walls. The bright yellow solution and fine white solids were allowed to settle before filtration through a glass microfibre filter disc. Concentration of the bright yellow supernatant to *ca*. 1 mL gave a large quantity of yellow solids which were heated into solution and allowed to cool slowly to room temperature to give large yellow blocks of **1Sc**. This mixture was stored at 5°C for 2 hours followed by –30°C for 16 hours to increase the yield. Crystals were isolated by decanting the supernatant followed by drying *in vacuo* (10^{-3} mbar, 2 hours). A second crop was obtained in a similar fashion (combined yield = 1.329 g, 57%).

Elemental analysis on $C_{72}H_{100}IN_2Sc\cdot(C_7H_8)_n$ for n = 2 calc. (%): C = 76.529, H = 8.663, N = 2.076; for n = 0 calc. (%): C = 74.201, H = 8.649, N = 2.404; found (%): C = 69.90, H = 8.44, N = 2.07 – low carbon values were found across duplicate samples.

^{1}H NMR ([D]$_6$-benzene, 400.13 MHz 298 K): δ = 7.33 (s, 8H, Tripp-3,5-*H*), 6.97 (d, $^3J_{HH}$ = 7.3 Hz, 4H, Ar-3,5-*H*), 6.69, (t, $^3J_{HH}$ = 7.4 Hz, 2H, Ar-4-*H*), 5.64 (s, 2H, ScN(*H*)), 3.01 (hept, $^3J_{HH}$ = 7.0 Hz, 8H, Tripp-2,6-C*H*(CH$_3$)$_2$), 2.66 (hept, $^3J_{HH}$ = 7.2 Hz, 4H, Tripp-4-C*H*(CH$_3$)$_2$), 1.40 (d, $^3J_{HH}$ = 6.9 Hz, 24H, Tripp-4-CH(C*H*$_3$)$_2$), 1.32 (d, $^3J_{HH}$ = 6.9 Hz, 24H, Tripp-2,6-CH(C*H*$_3$)$_2$), 1.11 (d, $^3J_{HH}$ = 6.9 Hz, 24H, Tripp-2,6-CH(C*H*$_3$)$_2$).

^{13}C{^{1}H} NMR ([D]$_6$-benzene, 100.62 MHz, 298 K): δ = 155.18 (Ar-*C*N(H)-Sc), 149.69 (Tripp-*ipso*-*C*), 148.71 (Tripp-2,6-*C*), 148.08 (Ar-2,6-*C*), 131.59 (Tripp-4-*C*), 127.10 (Ar-3,5-*C*H), 123.47 (Tripp-3,5-*C*H), 116.32 (Ar-4-*C*H), 34.03 (Tripp-4-*C*H(CH$_3$)$_2$), 31.28 (Tripp-2,6-*C*H(CH$_3$)$_2$), 25.96 (Tripp-4-CH(*C*H$_3$)$_2$), 24.34 (Tripp-2,6-CH(*C*H$_3$)$_2$), 24.10 (Tripp-2,6-CH(*C*H$_3$)$_2$).

UV-Vis-NIR (Et$_2$O): λ_{max} (cm^{-1}; ε) = A broad feature peak extends from ~500 nm (20,000 cm^{-1}) into the UV region, and beyond our spectral range.

FT-IR (ATR, microcrystalline): cm^{-1} = 3,482 (vs), 3,383 (vs), 3,284 (vs), 3,198 (vs), 3,052 (s), 3,021 (vs), 2,957 (vw), 2,927 (w), 2,867 (w), 2,754 (vs), 1,761 (vs), 1,603 (m), 1,585 (s), 1,574 (s), 1,566 (s), 1,541 (vs), 1,459 (vw), 1,441 (w), 1,406 (vw), 1,381 (vw), 1,361 (vw), 1,319 (w), 1,258 (vw), 1,243 (vw), 1,233 (vw), 1,188 (s), 1,163 (m), 1,153 (s), 1,126 (s), 1,097 (w), 1,077 (vw), 1,056 (m), 1,036 (m), 1,007 (m), 956 (s), 939 (m), 923 (s), 900 (s), 876 (vw), 863 (vw), 845 (w), 830 (w), 795 (w), 777 (m), 752 (vw), 730 (m), 695 (s), 668 (w), 652 (w), 635 (m), 619 (w), 602 (w), 586 (vw), 551 (m), 534 (m), 514 (w), 504 (m), 487 (m), 473 (m), 464 (m), 452 (m), 442 (m), 430 (m), 419 (m).

Synthesis of [Sc(NHAr^{iPr6})$_2$] (2Sc). Et_2O (15 mL) was added to a pre-cooled (–98°C) stirring mixture of solid **1Sc** (0.583 g, 0.5 mmol) and KC_8 (0.083 g, 0.6 mmol, 1.2 equiv.) in a glass Schlenk vessel equipped with a glass-coated stirrer bar. The mixture was allowed to slowly warm to room temperature while submerged in a cooling bath, during which time it became significantly darker, from a yellow mixture to a dark brown/black mixture. After stirring for 2 hours, the cooling bath had warmed to *ca*. 0°C, at which point the vessel was removed and allowed to warm up to room temperature with stirring for 15-20 minutes. The fine grey suspension, presumably a mixture of graphite, KI, and excess KC_8, was allowed to settle at room temperature, and the dark solution was filtered through a glass microfibre filter disc. The volatiles were removed *in vacuo* (10^{-3} mbar) which left a slightly sticky dark blue powder. Hexane (3 mL) was added with manual agitation to loosen solids from the vessel walls. The dark blue solution was filtered through a glass microfibre filter disc, concentrated to *ca.* 1 mL, and stored at –30°C for 16 hours which afforded a crop of dichroic red/green planks which were dried *in vacuo* (10^{-3} mbar, 1 hour). Yield = 1.368 g, 26%.

Elemental analysis on $C_{72}H_{100}N_2Sc$ calc. (%): C = 83.268, H = 9.705, N = 2.697; found (%): C = 79.89, H = 9.60, N = 2.54.

^{1}H NMR ([D]$_6$-benzene, 400.13 MHz, 298 K): Only peaks attributable to diamagnetic impurities could be identified.

UV-Vis-NIR (Et_2O): λ_{max} (cm^{-1}; ε) = 756 (13,412, 805), 575 (17,394, 1,820), 469 (21,315, 2,471) – note that these peaks are fairly broad. The positions and ε values here result from fitting each broad feature to a single Gaussian curve.

FT-IR (ATR, microcrystalline): cm^{-1} = 3,334 (vs), 3,042 (vs), 3,023 (vs), 2,957 (vw), 2,925 (w), 2,865 (w), 2,750 (vs), 2,721 (vs), 2,705 (vs), 1,605 (s), 1,583 (s), 1,566 (s), 1,527 (vs), 1,459 (w), 1,408 (vw), 1,381 (vw), 1,361 (vw), 1,317 (w), 1,264 (vw), 1,248 (vw), 1,188 (s), 1,163 (m), 1,126 (s), 1,100 (m), 1,073 (vw), 1,001 (m), 956 (s), 937 (m), 923 (s), 873 (vw),

855 (vw), 847 (vw), 830 (w), 789 (w), 769 (s), 746 (vw), 699 (s), 662 (w), 594 (w), 547 (w), 522 (m), 506 (w), 493 (m), 483 (m), 467 (m), 440 (m), 420 (m).

Density functional theory calculations

Unrestricted Kohn-Sham calculations were performed on S = ½ complexes [M(NHAr$^{i\text{Pr6}}$)$_2$] (**2M**, M = Sc, Y, La), S = 3 [Sm(NHAr$^{i\text{Pr6}}$)$_2$] (**2Sm**), S = $^7/_2$ [Eu(NHAr$^{i\text{Pr6}}$)$_2$] (**2Eu**), S = $^1/_2$ [Tm(NHAr$^{i\text{Pr6}}$)$_2$] (**2Tm**), and S = 0 [Yb(NHAr$^{i\text{Pr6}}$)$_2$] (**2Yb**) at the DFT level using the ORCA 5.0 quantum chemistry program suite.[85] Partial geometry optimisations were performed using the TPSSh hybrid meta-generalized gradient density functional (meta-GGA)[86,87] with Grimme's D3BJ dispersion correction,[88,89] and the resolution of the identity 'chain of spheres' (RIJCOSX) approximation.[90,91] Elements Y, La, Sm, Eu, Tm, and Yb were treated with a segmented all-electron relativistically contracted (SARC) Dougless-Kroll-Hess second order (DKH-def2) basis set at the triple-ζ level (SARC-DKH-TZVP),[92] Sc was treated with a DKH-def2 basis set at the triple-ζ level (DKH-def2-TZVP),[93] while a split-valence polarized basis set (DKH-def2-SVP) was used for all other atoms.[93] A SARC/J auxiliary basis set was used for each atom type as appropriate.[92,94] No symmetry constraints were imposed. Occasionally the SlowConv switch was used to ensure SCF convergence, along with the DefGrid3 (tight integration grid) switch.

For property calculations additional functionals (B3PW91,[95] CAM-B3LYP,[96] PBE,[97,98] PBE0,[99,100] TPSSh[86,87], TPSS0[101]) and alternative relativistic treatments (DKH, and ZORA – Zeroth Order Regular Approximation) were investigated,[102-104] along with the use of larger basis sets on all atoms at either the triple-ζ (H, C, N) or quadruple-ζ (Sc, Y, La) level and with additional polarization functions as appropriate. The basis sets used were as follows: H, C, N (DKH/ZORA-def2-TZVP); Sc (ma-DKH/ZORA-def2-QZVPP); Y (SARC-DKH/ZORA-

TZVPP); also Sc, Y (Sapporo-DKH3-QZP-2012);[105] La, Sm, Eu, Tm, Yb (SARC2-DKH/ZORA-QZVP).[106] All were used with their default settings within ORCA 5.0.4.[85]

Complete active space self-consistent field calculations

CASSCF calculations were performed with OpenMolcas v21.06.[107] (Partially) DFT-optimized structures were used in all cases: H-atoms optimized for **2Sc**, **2Y**, **2Sm**, **2Eu** (1st structure in asymmetric unit), **2Tm** and **2Yb** (1st structure in asymmetric unit); while for **2La** the six C-atoms of the distorted Tripp arene ring along with all atoms of the 4-*i*Pr group and all H-atoms in the structure were optimized; and **2Y-Et$_2$O** the whole structure was optimized as described. Basis sets from the ANO-RCC library were employed,[108-111] with VTZP quality for the metal atom, VDZP quality for the 12 arene ring carbon atoms and the nitrogen atoms, while VDZ quality was employed for all other atoms. Cholesky decomposition of the two-electron integrals to a threshold of 10^{-8} was performed, along with employing the 2nd order Douglass-Kroll-Hess transformation to account for scalar relativistic effects.[112] MC-PDFT corrections were made in some cases.[113,114] For **2Sc**, **2Y**, **2Y-Et$_2$O** and **2La** the active space was one electron in the four lowest-lying metal-based orbitals (corresponding to the excitations discussed in the text), while for **2Sm**, **2Eu** and **2Tm** the active space was six, seven and thirteen electrons, respectively, in seven 4f orbitals. We performed state average CASSCF calculations for four doublet roots for **2Sc**, **2Y**, **2Y-Et$_2$O** and **2La**, while for **2Sm** we considered seven septets, for **2Eu** we considered one octet and 48 sextets, and for **2Tm** we considered seven doublets. For **2Yb** we started with a restricted Hartree-Fock calculation and performed RAS-probing calculations for four doublet roots, including frontier orbitals (11 orbitals in Ras1 and 5 orbitals in Ras3) and single excitations, finding a $4f^{14}$ ground state. No indication of low-lying nd^1 or ligand radical configurations arose in any of **2Sm**, **2Eu**, **2Tm** or **2Yb**.

Electron paramagnetic resonance spectroscopy

Cw EPR spectra were recorded using a Bruker EMX 300 EPR spectrometer operating at X–band frequency (ca. 9.8 GHz) and a Bruker EMX Micro EPR spectrometer operating at X–band frequency (ca. 9.4 GHz). Temperature variation and control were achieved using a Stinger closed-cycle helium gas cryostat (10 – 180 K) or the Bruker ER 4131VT-M liquid nitrogen cryostat (130 – 250 K).

References

(1) Bochkarev, M. N. Molecular compounds of “new” divalent lanthanides. *Coord. Chem. Rev.* **2004**, *248* (9-10), 835-851. DOI: https://doi.org/10.1016/j.ccr.2004.04.004

(2) Platt, A. W. G. Divalent Lanthanides in Solution. In *Encyclopedia of Inorganic and Bioinorganic Chemistry*, 2004; pp 1-6.

(3) Nief, F. Non-classical divalent lanthanide complexes. *Dalton Trans.* **2010**, *39* (29), 6589-6598. DOI: https://doi.org/10.1039/C001280G

(4) Cotton, S. *Lanthanide and Actinide Chemistry*; John Wiley & Sons, Ltd, 2006. DOI: https://doi.org/10.1002/0470010088.

(5) Szostak, M.; Fazakerley, N. J.; Parmar, D.; Procter, D. J. Cross-coupling reactions using samarium(II) iodide. *Chem. Rev.* **2014**, *114* (11), 5959-6039. DOI: https://doi.org/10.1021/cr400685r

(6) Szostak, M.; Procter, D. J. Beyond samarium diiodide: vistas in reductive chemistry mediated by lanthanides(II). *Angew. Chem., Int. Ed.* **2012**, *51* (37), 9238-9256. DOI: https://doi.org/10.1002/anie.201201065

(7) Edmonds, D. J.; Johnston, D.; Procter, D. J. Samarium(II)-iodide-mediated cyclizations in natural product synthesis. *Chem. Rev.* **2004**, *104* (7), 3371-3404. DOI: https://doi.org/10.1021/cr030017a

(8) Morss, L. R. Thermochemical properties of yttrium, lanthanum, and the lanthanide elements and ions. *Chem. Rev.* **1976**, *76* (6), 827-841. DOI: https://doi.org/10.1021/cr60304a007

(9) Szostak, M.; Spain, M.; Procter, D. J. Uncovering the importance of proton donors in TmI_2-promoted electron transfer: facile C-N bond cleavage in unactivated amides. *Angew. Chem., Int. Ed.* **2013**, *52* (28), 7237-7241. DOI: https://doi.org/10.1002/anie.201303178

(10) Evans, W. J.; Allen, N. T.; Ziller, J. W. The Availability of Dysprosium Diiodide as a Powerful Reducing Agent in Organic Synthesis: Reactivity Studies and Structural Analysis of $DyI_2(DME)_3$ and Its Naphthalene Reduction Product. *J. Am. Chem. Soc.* **2000**, *122* (47), 11749-11750. DOI: https://doi.org/10.1021/ja0034949

(11) Bochkarev, M. N.; Fedushkin, I. L.; Dechert, S.; Fagin, A. A.; Schumann, H. $[NdI_2(thf)_5]$, the First Crystallographically Authenticated Neodymium(II) Complex. *Angew. Chem., Int. Ed.* **2001**, *40* (17), 3176-3178. DOI: https://doi.org/10.1002/1521-3773(20010903)40:17%3C3176::AID-ANIE3176%3E3.0.CO;2-Y

(12) Bochkarev, M. N.; Fagin, A. A. A New Route to Neodymium(II) and Dysprosium(II) Iodides. *Chem. Eur. J.* **1999**, *5* (10), 2990-2992. DOI: https://doi.org/10.1002/(SICI)1521-3765(19991001)5:10%3C2990::AID-CHEM2990%3E3.0.CO;2-U

(13) Bochkarev, M. N.; Fedushkin, I. L.; Fagin, A. A.; Petrovskaya, T. V.; Ziller, J. W.; Broomhall-Dillard, R. N. R.; Evans, W. J. Synthesis and Structure of the First Molecular Thulium(II) Complex: $[TmI_2(MeOCH_2CH_2OMe)_3]$. *Angew. Chem., Int. Ed.* **1997**, *36* (12), 133-135. DOI: https://doi.org/10.1002/anie.199701331

(14) Meyer, G. Reduced halides of the rare-earth elements. *Chem. Rev.* **2002**, *88* (1), 93-107. DOI: https://doi.org/10.1021/cr00083a005

(15) Meyer, G. Small cause ‐ Great effect: What the $4f^{n+1}5d^0 \rightarrow 4f^n5d^1$ configuration crossover does to the chemistry of divalent rare-earth halides and coordination compounds. *Journal of Solid State Chemistry* **2019**, *270*, 324-334. DOI: https://doi.org/10.1016/j.jssc.2018.10.050

(16) Nugent, L. J. Standard electrode potentials and enthalpies of formation of some lanthanide and actinide aquo-ions. *J. Inorg. Nucl. Chem.* **1975**, *37* (7-8), 1767-1770. DOI: https://doi.org/10.1016/0022-1902(75)80314-9

(17) Evans, W. J. Tutorial on the Role of Cyclopentadienyl Ligands in the Discovery of Molecular Complexes of the Rare-Earth and Actinide Metals in New Oxidation States. *Organometallics* **2016**, *35* (18), 3088-3100. DOI: https://doi.org/10.1021/acs.organomet.6b00466

(18) Jin, P.-B.; Luo, Q.-C.; Gransbury, G. K.; Vitorica-Yrezabal, I. J.; Hajdu, T.; Strashnov, I.; McInnes, E. J. L.; Winpenny, R. E. P.; Chilton, N. F.; Mills, D. P.; Zheng, Y.-Z. Thermally Stable Terbium(II) and Dysprosium(II) Bis-amidinate Complexes. *J. Am. Chem. Soc.* **2023**, *145* (51), 27993-28009. DOI: https://doi.org/10.1021/jacs.3c07978

(19) Meihaus, K. R.; Fieser, M. E.; Corbey, J. F.; Evans, W. J.; Long, J. R. Record High Single-Ion Magnetic Moments Through $4f^n5d^1$ Electron Configurations in the Divalent Lanthanide Complexes $[(C_5H_4SiMe_3)_3Ln]^-$. *J. Am. Chem. Soc.* **2015**, *137* (31), 9855-9860. DOI: https://doi.org/10.1021/jacs.5b03710

(20) Huh, D. N.; Ciccone, S. R.; Bekoe, S.; Roy, S.; Ziller, J. W.; Furche, F.; Evans, W. J. Synthesis of Ln^{II} -in-Cryptand Complexes by Chemical Reduction of Ln^{III} -in-Cryptand Precursors: Isolation of a Nd^{II} -in-Cryptand Complex. *Angew. Chem., Int. Ed.* **2020**, *59* (37), 16141-16146. DOI: https://doi.org/10.1002/anie.202006393

(21) MacDonald, M. R.; Ziller, J. W.; Evans, W. J. Synthesis of a crystalline molecular complex of Y^{2+}, [(18-crown-6)K][$(C_5H_4SiMe_3)_3Y$]. *J. Am. Chem. Soc.* **2011**, *133* (40), 15914-15917. DOI: https://doi.org/10.1021/ja207151y

(22) MacDonald, M. R.; Bates, J. E.; Fieser, M. E.; Ziller, J. W.; Furche, F.; Evans, W. J. Expanding rare-earth oxidation state chemistry to molecular complexes of holmium(II) and erbium(II). *J. Am. Chem. Soc.* **2012**, *134* (20), 8420-8423. DOI: https://doi.org/10.1021/ja303357w

(23) MacDonald, M. R.; Bates, J. E.; Ziller, J. W.; Furche, F.; Evans, W. J. Completing the series of +2 ions for the lanthanide elements: synthesis of molecular complexes of

Pr^{2+}, Gd^{2+}, Tb^{2+}, and Lu^{2+}. *J. Am. Chem. Soc.* **2013**, *135* (26), 9857-9868. DOI: https://doi.org/10.1021/ja403753j

(24) Fieser, M. E.; Ferrier, M. G.; Su, J.; Batista, E.; Cary, S. K.; Engle, J. W.; Evans, W. J.; Lezama Pacheco, J. S.; Kozimor, S. A.; Olson, A. C.; Ryan, A. J.; Stein, B. W.; Wagner, G. L.; Woen, D. H.; Vitova, T.; Yang, P. Evaluating the electronic structure of formal Ln^{II} ions in $Ln^{II}(C_5H_4SiMe_3)_3^{1-}$ using XANES spectroscopy and DFT calculations. *Chem. Sci.* **2017**, *8* (9), 6076-6091. DOI: https://doi.org/10.1039/C7SC00825B

(25) Trinh, M. T.; Wedal, J. C.; Evans, W. J. Evaluating electrochemical accessibility of $4f^n5d^1$ and $4f^{n+1}$ Ln(II) ions in $(C_5H_4SiMe_3)_3Ln$ and $(C_5Me_4H)_3Ln$ complexes. *Dalton Trans.* **2021**, *50* (40), 14384-14389. DOI: https://doi.org/10.1039/D1DT02427B

(26) Gould, C. A.; McClain, K. R.; Reta, D.; Kragskow, J. G. C.; Marchiori, D. A.; Lachman, E.; Choi, E. S.; Analytis, J. G.; Britt, R. D.; Chilton, N. F.; Harvey, B. G.; Long, J. R. Ultrahard magnetism from mixed-valence dilanthanide complexes with metal-metal bonding. *Science* **2022**, *375* (6577), 198-202. DOI: https://doi.org/10.1126/science.abl5470

(27) Jenkins, T. F.; Woen, D. H.; Mohanam, L. N.; Ziller, J. W.; Furche, F.; Evans, W. J. Tetramethylcyclopentadienyl Ligands Allow Isolation of Ln(II) Ions across the Lanthanide Series in $[K(2.2.2\text{-cryptand})][(C_5Me_4H)_3Ln]$ Complexes. *Organometallics* **2018**, *37* (21), 3863-3873. DOI: https://doi.org/10.1021/acs.organomet.8b00557

(28) Ryan, A. J.; Darago, L. E.; Balasubramani, S. G.; Chen, G. P.; Ziller, J. W.; Furche, F.; Long, J. R.; Evans, W. J. Synthesis, Structure, and Magnetism of Tris(amide) $[Ln\{N(SiMe_3)_2\}_3]^{1-}$ Complexes of the Non-traditional +2 Lanthanide Ions. *Chem. Eur. J.* **2018**, *24* (30), 7702-7709. DOI: https://doi.org/10.1002/chem.201800610

(29) Kundu, K.; White, J. R. K.; Moehring, S. A.; Yu, J. M.; Ziller, J. W.; Furche, F.; Evans, W. J.; Hill, S. A 9.2-GHz clock transition in a Lu(II) molecular spin qubit arising from a

3,467-MHz hyperfine interaction. *Nat. Chem.* **2022**, *14* (4), 392-397. DOI: https://doi.org/10.1038/s41557-022-00894-4

(30) Anderson-Sanchez, L. M.; Yu, J. M.; Ziller, J. W.; Furche, F.; Evans, W. J. Room-Temperature Stable Ln(II) Complexes Supported by 2,6-Diadamantyl Aryloxide Ligands. *Inorg. Chem.* **2023**, *62* (2), 706-714. DOI: https://doi.org/10.1021/acs.inorgchem.2c02167

(31) McClain, K. R.; Gould, C. A.; Marchiori, D. A.; Kwon, H.; Nguyen, T. T.; Rosenkoetter, K. E.; Kuzmina, D.; Tuna, F.; Britt, R. D.; Long, J. R.; Harvey, B. G. Divalent Lanthanide Metallocene Complexes with a Linear Coordination Geometry and Pronounced 6s-5d Orbital Mixing. *J. Am. Chem. Soc.* **2022**, *144* (48), 22193-22201. DOI: https://doi.org/10.1021/jacs.2c09880

(32) Moehring, S. A.; Miehlich, M.; Hoerger, C. J.; Meyer, K.; Ziller, J. W.; Evans, W. J. A Room-Temperature Stable Y(II) Aryloxide: Using Steric Saturation to Kinetically Stabilize Y(II) Complexes. *Inorg. Chem.* **2020**, *59* (5), 3207-3214. DOI: https://doi.org/10.1021/acs.inorgchem.9b03587

(33) Fieser, M. E.; MacDonald, M. R.; Krull, B. T.; Bates, J. E.; Ziller, J. W.; Furche, F.; Evans, W. J. Structural, spectroscopic, and theoretical comparison of traditional vs recently discovered Ln^{2+} ions in the [K(2.2.2-cryptand)][$(C_5H_4SiMe_3)_3Ln$] complexes: the variable nature of Dy^{2+} and Nd^{2+}. *J. Am. Chem. Soc.* **2015**, *137* (1), 369-382. DOI: https://doi.org/10.1021/ja510831n

(34) Gould, C. A.; McClain, K. R.; Yu, J. M.; Groshens, T. J.; Furche, F.; Harvey, B. G.; Long, J. R. Synthesis and Magnetism of Neutral, Linear Metallocene Complexes of Terbium(II) and Dysprosium(II). *J. Am. Chem. Soc.* **2019**, *141* (33), 12967-12973. DOI: https://doi.org/10.1021/jacs.9b05816

(35) Fleischauer, V. E.; Ganguly, G.; Woen, D. H.; Wolford, N. J.; Evans, W. J.; Autschbach, J.; Neidig, M. L. Insight into the Electronic Structure of Formal

Lanthanide(II) Complexes using Magnetic Circular Dichroism Spectroscopy. *Organometallics* **2019**, *38* (16), 3124-3131. DOI: https://doi.org/10.1021/acs.organomet.9b00315

(36) MacDonald, M. R.; Fieser, M. E.; Bates, J. E.; Ziller, J. W.; Furche, F.; Evans, W. J. Identification of the +2 oxidation state for uranium in a crystalline molecular complex, [K(2.2.2-cryptand)][($C_5H_4SiMe_3$)$_3$U]. *J. Am. Chem. Soc.* **2013**, *135* (36), 13310-13313. DOI: https://doi.org/10.1021/ja406791t

(37) Hitchcock, P. B.; Lappert, M. F.; Maron, L.; Protchenko, A. V. Lanthanum does form stable molecular compounds in the +2 oxidation state. *Angew. Chem., Int. Ed.* **2008**, *47* (8), 1488-1491. DOI: https://doi.org/10.1002/anie.200704887

(38) Ariciu, A.-M.; Woen, D. H.; Huh, D. N.; Nodaraki, L. E.; Kostopoulos, A. K.; Goodwin, C. A. P.; Chilton, N. F.; McInnes, E. J. L.; Winpenny, R. E. P.; Evans, W. J.; Tuna, F. Engineering electronic structure to prolong relaxation times in molecular qubits by minimising orbital angular momentum. *Nat. Commun.* **2019**, *10* (1), 3330. DOI: https://doi.org/10.1038/s41467-019-11309-3

(39) Dorenbos, P. f→d transition energies of divalent lanthanides in inorganic compounds. *J. Condens. Matter Phys.* **2003**, *15* (3), 575-594. DOI: https://doi.org/10.1088/0953-8984/15/3/322

(40) Dorenbos, P. The $4f^n \leftrightarrow 4f^{n-1}5d$ transitions of the trivalent lanthanides in halogenides and chalcogenides. *Journal of Luminescence* **2000**, *91* (1), 91-106. DOI: https://doi.org/10.1016/S0022-2313(00)00197-6

(41) Beck, H. P. Notizen: NdI2-II, eine metallisch leitende Hochdruckmodifikation ? / NdI2, a Metallic High Pressure Modification ? *Z. Naturforsch. B* **1976**, *31* (11), 1548-1549. DOI: https://doi.org/10.1515/znb-1976-1128

(42) Fieser, M. E.; Palumbo, C. T.; La Pierre, H. S.; Halter, D. P.; Voora, V. K.; Ziller, J. W.; Furche, F.; Meyer, K.; Evans, W. J. Comparisons of lanthanide/actinide +2 ions in a

tris(aryloxide)arene coordination environment. *Chem. Sci.* **2017**, *8* (11), 7424-7433. DOI: https://doi.org/10.1039/C7SC02337E

(43) Simon, A.; Mattausch, H.; Ryazanov, M.; Kremer, R. K. Lanthanides as d Metals. *Z. Anorg. Allg. Chem.* **2006**, *632* (6), 919-929. DOI: https://doi.org/10.1002/zaac.200500506

(44) McClain, K. R.; Kwon, H.; Chakarawet, K.; Nabi, R.; Kragskow, J. G. C.; Chilton, N. F.; Britt, R. D.; Long, J. R.; Harvey, B. G. A Trinuclear Gadolinium Cluster with a Three-Center One-Electron Bond and an S = 11 Ground State. *J. Am. Chem. Soc.* **2023**, *145* (16), 8996-9002. DOI: https://doi.org/10.1021/jacs.3c00182

(45) Wedal, J. C.; Anderson-Sanchez, L. M.; Dumas, M. T.; Gould, C. A.; Beltran-Leiva, M. J.; Celis-Barros, C.; Paez-Hernandez, D.; Ziller, J. W.; Long, J. R.; Evans, W. J. Synthesis and Crystallographic Characterization of a Reduced Bimetallic Yttrium ansa-Metallocene Hydride Complex, [K(crypt)][(mu-Cp(An))Y(mu-H)](2) (Cp(An) = Me(2)Si[C(5)H(3)(SiMe(3))-3](2)), with a 3.4 A Yttrium-Yttrium Distance. *J. Am. Chem. Soc.* **2023**, *145* (19), 10730-10742. DOI: https://doi.org/10.1021/jacs.3c01405

(46) Smith, P. W.; Hrubý, J.; Evans, W. J.; Hill, S.; Minasian, S. G. Identification of an X-Band Clock Transition in Cp′ 3Pr⁻ Enabled by a 4f25d1 Configuration. *J. Am. Chem. Soc.* **2024**. DOI: https://doi.org/10.1021/jacs.3c12725

(47) Jin, P.-B.; Luo, Q.-C.; Gransbury, G.; Vitorica-Yrezabal, I.; Hajdu, T.; McInnes, E.; Winpenny, R.; Chilton, N.; Mills, D.; Zheng, Y.-Z. Thermally stable Terbium(II) and Dysprosium(II) Bis-Amidinate Single-Molecule Magnets. *ChemRxiv* **2023**. DOI: ***https://doi.org/10.26434/chemrxiv-2023-snc7m***

(48) Straub, M. D.; Ouellette, E. T.; Boreen, M. A.; Britt, R. D.; Chakarawet, K.; Douair, I.; Gould, C. A.; Maron, L.; Del Rosal, I.; Villarreal, D.; Minasian, S. G.; Arnold, J. A Uranium(II) Arene Complex That Acts as a Uranium(I) Synthon. *J. Am. Chem. Soc.* **2021**, *143* (47), 19748-19760. DOI: https://doi.org/10.1021/jacs.1c07854

(49) Cryer, J. D.; Liddle, S. T. 4.08 - Arene Complexes of the Actinides. In *Comprehensive Organometallic Chemistry IV*, Parkin, G., Meyer, K., O'hare, D. Eds.; Elsevier, 2022; pp 460-501.

(50) Murillo, J.; Bhowmick, R.; Harriman, K. L. M.; Gomez-Torres, A.; Wright, J.; Meulenberg, R. W.; Miro, P.; Metta-Magana, A.; Murugesu, M.; Vlaisavljevich, B.; Fortier, S. Actinide arene-metalates: ion pairing effects on the electronic structure of unsupported uranium-arenide sandwich complexes. *Chem. Sci.* **2021**, *12* (40), 13360-13372. DOI: https://doi.org/10.1039/D1SC03275E

(51) Keerthi Shivaraam, R. A.; Keener, M.; Modder, D. K.; Rajeshkumar, T.; Zivkovic, I.; Scopelliti, R.; Maron, L.; Mazzanti, M. A Route to Stabilize Uranium(II) and Uranium(I) Synthons in Multimetallic Complexes. *Angew. Chem., Int. Ed.* **2023**, *62* (23), e202304051. DOI: https://doi.org/10.1002/anie.202304051

(52) Keener, M.; Shivaraam, R. A. K.; Rajeshkumar, T.; Tricoire, M.; Scopelliti, R.; Zivkovic, I.; Chauvin, A. S.; Maron, L.; Mazzanti, M. Multielectron Redox Chemistry of Uranium by Accessing the +II Oxidation State and Enabling Reduction to a U(I) Synthon. *J. Am. Chem. Soc.* **2023**, *145* (29), 16271-16283. DOI: https://doi.org/10.1021/jacs.3c05626

(53) La Pierre, H. S.; Scheurer, A.; Heinemann, F. W.; Hieringer, W.; Meyer, K. Synthesis and characterization of a uranium(II) monoarene complex supported by δ backbonding. *Angew. Chem., Int. Ed.* **2014**, *53* (28), 7158-71562. DOI: https://doi.org/10.1002/anie.201402050

(54) Brennan, J. G.; Cloke, F. G. N.; Sameh, A. A.; Zalkin, A. Synthesis of bis(η-1,3,5-tri-t-butylbenzene) sandwich complexes of yttrium(0) and gadolinium(0); the X-ray crystal structure of the first authentic lanthanide(0) complex, [Gd(η-$Bu^t_3C_6H_3)_2$]. *J. Chem. Soc., Chem. Commun.* **1987**, (21), 1668-1669. DOI: https://doi.org/10.1039/C39870001668

(55) Anderson, D. M.; Cloke, F. G. N.; Cox, P. A.; Edelstein, N.; Green, J. C.; Pang, T.; Sameh, A. A.; Shalimoff, G. On the stability and bonding in bis(η-arene)lanthanide complexes. *J. Chem. Soc., Chem. Commun.* **1989**, (1), 53-55. DOI: https://doi.org/10.1039/C39890000053

(56) King, W. A.; Marks, T. J.; Anderson, D. M.; Duncalf, D. J.; Cloke, F. G. N. Organo-f-element bonding energetics. Large magnitudes of metal arene bond enthalpies in zero-valent lanthanide sandwich complexes. *J. Am. Chem. Soc.* **1992**, *114* (23), 9221-9223. DOI: https://doi.org/10.1021/ja00049a084

(57) Cloke, F. G. N. Zero oxidation state compounds of scandium, yttrium, and the lanthanides. *Chem. Soc. Rev.* **1993**, *22* (1), 17-24. DOI: https://doi.org/10.1039/CS9932200017

(58) King, W. A.; Di Bella, S.; Lanza, G.; Khan, K.; Duncalf, D. J.; Cloke, F. G. N.; Fragala, I. L.; Marks, T. J. Metal−Ligand Bonding and Bonding Energetics in Zerovalent Lanthanide, Group 3, Group 4, and Group 6 Bis(arene) Sandwich Complexes. A Combined Solution Thermochemical and ab Initio Quantum Chemical Investigation. *J. Am. Chem. Soc.* **1996**, *118* (3), 627-635. DOI: https://doi.org/10.1021/ja9529697

(59) Jena, R.; Benner, F.; Delano, F.; Holmes, D.; McCracken, J.; Demir, S.; Odom, A. L. A rare isocyanide derived from an unprecedented neutral yttrium(II) bis(amide) complex. *Chem. Sci.* **2023**, *14* (16), 4257-4264. DOI: https://doi.org/10.1039/D3SC00171G

(60) Billow, B. S.; Livesay, B. N.; Mokhtarzadeh, C. C.; McCracken, J.; Shores, M. P.; Boncella, J. M.; Odom, A. L. Synthesis and Characterization of a Neutral U(II) Arene Sandwich Complex. *J. Am. Chem. Soc.* **2018**, *140* (50), 17369-17373. DOI: https://doi.org/10.1021/jacs.8b10888

(61) Barnett, B. R.; Mokhtarzadeh, C. C.; Lummis, P.; Wang, S.; Queen, J. D.; Gavenonis, J.; Schüwer, N.; Tilley, T. D.; Boynton, J. N.; Weidemann, N.; Agnew, D. W.; Smith, P.

W.; Ditri, T. B.; Carpenter, A. E.; Pratt, J. K.; Mendelson, N. D.; Figueroa, J. S.; Power, P. P. TERPHENYL LIGANDS AND COMPLEXES. In *Inorganic Syntheses*, Inorganic Syntheses, 2018; pp 85-122.

(62) Twamley, B.; Hwang, C.-S.; Hardman, N. J.; Power, P. P. Sterically encumbered terphenyl substituted primary pnictanes $ArEH_2$ and their metallated derivatives ArE(H)Li (Ar = $–C_6H_3$-2,6-$Trip_2$; Trip = 2,4,6-triisopropylphenyl; E=N, P, As, Sb). *J. Organomet. Chem.* **2000**, *609* (1-2), 152-160. DOI: https://doi.org/10.1016/S0022-328X(00)00162-5

(63) Izod, K.; Liddle, S. T.; Clegg, W. A convenient route to lanthanide triiodide THF solvates. Crystal structures of $LnI_3(THF)_4$ [Ln = Pr] and $LnI_3(THF)_{3.5}$ [Ln = Nd, Gd, Y]. *Inorg. Chem.* **2004**, *43* (1), 214-218. DOI: https://doi.org/10.1021/ic034851u

(64) Girard, P.; Namy, J. L.; Kagan, H. B. Divalent lanthanide derivatives in organic synthesis. 1. Mild preparation of samarium iodide and ytterbium iodide and their use as reducing or coupling agents. *J. Am. Chem. Soc.* **1980**, *102* (8), 2693-2698. DOI: https://doi.org/10.1021/ja00528a029

(65) Liu, J.; Bollmeyer, M. M.; Kim, Y.; Xiao, D.; MacMillan, S. N.; Chen, Q.; Leng, X.; Kim, S. H.; Zhao, L.; Lancaster, K. M.; Deng, L. An Isolable Mononuclear Palladium(I) Amido Complex. *J. Am. Chem. Soc.* **2021**, *143* (28), 10751-10759. DOI: https://doi.org/10.1021/jacs.1c04965

(66) Shannon, R. D. Revised effective ionic radii and systematic studies of interatomic distances in halides and chalcogenides. *Acta Crystallogr. A* **1976**, *32* (5), 751-767. DOI: https://doi.org/10.1107/s0567739476001551

(67) Chowdhury, S. R.; Goodwin, C. A. P.; Vlaisavljevich, B. What is the nature of the uranium(III)–arene bond? *Chem. Sci.* **2024**, (Advance Article). DOI: https://doi.org/10.1039/D3SC04715F

(68) Boynton, J. N.; Guo, J. D.; Grandjean, F.; Fettinger, J. C.; Nagase, S.; Long, G. J.; Power, P. P. Synthesis and characterization of the titanium bisamide Ti{N(H)Ar$^{i\text{Pr6}}$}$_2$ (Ar$^{i\text{Pr6}}$ = C$_6$H$_3$-2,6-(C$_6$H$_2$-2,4,6-^{i}Pr$_3$)$_2$ and its TiCl{N(H)Ar$^{i\text{Pr6}}$}$_2$ precursor: Ti(II) → Ti(IV) cyclization. *Inorg. Chem.* **2013**, *52* (24), 14216-14223. DOI: https://doi.org/10.1021/ic4021355

(69) Chilton, N. F.; Goodwin, C. A. P.; Mills, D. P.; Winpenny, R. E. P. The first near-linear bis(amide) f-block complex: a blueprint for a high temperature single molecule magnet. *Chem. Commun.* **2015**, *51* (1), 101-103. DOI: https://doi.org/10.1039/c4cc08312a

(70) Goodwin, C. A. P.; Joslin, K. C.; Lockyer, S. J.; Formanuik, A.; Morris, G. A.; Ortu, F.; Vitorica-Yrezabal, I. J.; Mills, D. P. Homoleptic Trigonal Planar Lanthanide Complexes Stabilized by Superbulky Silylamide Ligands. *Organometallics* **2015**, *34* (11), 2314-2325. DOI: https://doi.org/10.1021/om501123e

(71) Goodwin, C. A. P.; Chilton, N. F.; Vettese, G. F.; Moreno Pineda, E.; Crowe, I. F.; Ziller, J. W.; Winpenny, R. E. P.; Evans, W. J.; Mills, D. P. Physicochemical Properties of Near-Linear Lanthanide(II) Bis(silylamide) Complexes (Ln = Sm, Eu, Tm, Yb). *Inorg. Chem.* **2016**, *55* (20), 10057-10067. DOI: https://doi.org/10.1021/acs.inorgchem.6b00808

(72) Goodwin, C. A. P.; Chilton, N. F.; Natrajan, L. S.; Boulon, M.-E.; Ziller, J. W.; Evans, W. J.; Mills, D. P. Investigation into the Effects of a Trigonal-Planar Ligand Field on the Electronic Properties of Lanthanide(II) Tris(silylamide) Complexes (Ln = Sm, Eu, Tm, Yb). *Inorg. Chem.* **2017**, *56* (10), 5959-5970. DOI: https://doi.org/10.1021/acs.inorgchem.7b00664

(73) Carnall, W. T.; Fields, P. R. Lanthanide and Actinide Absorption Spectra in Solution. In *Lanthanide/Actinide Chemistry*, Advances in Chemistry, Vol. 71; American Chemical Society, 1967; pp 86-101.

(74) Takikawa, Y.; Ebisu, S.; Nagata, S. Van Vleck paramagnetism of the trivalent Eu ions. *Journal of Physics and Chemistry of Solids* **2010**, *71* (11), 1592-1598. DOI: https://doi.org/10.1016/j.jpcs.2010.08.006

(75) Bannwarth, C.; Grimme, S. A simplified time-dependent density functional theory approach for electronic ultraviolet and circular dichroism spectra of very large molecules. *Computational and Theoretical Chemistry* **2014**, *1040-1041*, 45-53. DOI: https://doi.org/10.1016/j.comptc.2014.02.023

(76) Barone, V.; Cossi, M. Quantum Calculation of Molecular Energies and Energy Gradients in Solution by a Conductor Solvent Model. *J. Phys. Chem. A* **1998**, *102* (11), 1995-2001. DOI: https://doi.org/10.1021/jp9716997

(77) Rajabi, A.; Grotjahn, R.; Rappoport, D.; Furche, F. A DFT perspective on organometallic lanthanide chemistry. *Dalton Trans.* **2024**, *53* (2), 410-417. DOI: https://doi.org/10.1039/D3DT03221C

(78) Palumbo, C. T.; Halter, D. P.; Voora, V. K.; Chen, G. P.; Chan, A. K.; Fieser, M. E.; Ziller, J. W.; Hieringer, W.; Furche, F.; Meyer, K.; Evans, W. J. Metal versus Ligand Reduction in Ln^{3+} Complexes of a Mesitylene-Anchored Tris(Aryloxide) Ligand. *Inorg. Chem.* **2018**, *57* (5), 2823-2833. DOI: https://doi.org/10.1021/acs.inorgchem.7b03236

(79) Queen, J. D.; Anderson-Sanchez, L. M.; Stennett, C. R.; Rajabi, A.; Ziller, J. W.; Furche, F.; Evans, W. J. Synthesis of Crystallographically Characterizable Bis(cyclopentadienyl) Sc(II) Complexes: $(C_5H_2{}^tBu_3)_2Sc$ and $\{[C_5H_3(SiMe_3)_2]_2ScI\}^{1-}$. *J. Am. Chem. Soc.* **2024**, *146* (5), 3279-3292. DOI: https://doi.org/10.1021/jacs.3c11922

(80) Morton, J. R.; Preston, K. F. Atomic parameters for paramagnetic resonance data. *Journal of Magnetic Resonance (1969)* **1978**, *30* (3), 577-582. DOI: https://doi.org/10.1016/0022-2364(78)90284-6

(81) Liu, J.; Nodaraki, L. E.; Martins, D. O. T. A.; Giansiracusa, M. J.; Cobb, P. J.; Emerson-King, J.; Ortu, F.; Whitehead, G. F. S.; Gransbury, G. K.; McInnes, E. J. L.; Tuna, F.; Mills, D. P. Non-Classical Early Lanthanide(II) Tris(di-tert-butylcyclopentadienyl) Complexes. *Eur. J. Inorg. Chem.* **2023**, *26* (36), e202300552. DOI: https://doi.org/10.1002/ejic.202300552

(82) Corbey, J. F.; Woen, D. H.; Palumbo, C. T.; Fieser, M. E.; Ziller, J. W.; Furche, F.; Evans, W. J. Ligand Effects in the Synthesis of Ln2+ Complexes by Reduction of Tris(cyclopentadienyl) Precursors Including C–H Bond Activation of an Indenyl Anion. *Organometallics* **2015**, *34* (15), 3909-3921. DOI: https://doi.org/10.1021/acs.organomet.5b00500

(83) Angadol, M. A.; Woen, D. H.; Windorff, C. J.; Ziller, J. W.; Evans, W. J. *tert*-Butyl(cyclopentadienyl) Ligands Will Stabilize Nontraditional +2 Rare-Earth Metal Ions. *Organometallics* **2019**, *38* (5), 1151-1158. DOI: https://doi.org/10.1021/acs.organomet.8b00941

(84) Moehring, S. A.; Evans, W. J. Evaluating Electron Transfer Reactivity of Rare-Earth Metal(II) Complexes Using EPR Spectroscopy. *Organometallics* **2020**, *39* (8), 1187-1194. DOI: https://doi.org/10.1021/acs.organomet.9b00837

(85) Neese, F. Software update: The ORCA program system—Version 5.0. *WIRES Comput. Mol. Sci.* **2022**, *12* (5). DOI: https://doi.org/10.1002/wcms.1606

(86) Staroverov, V. N.; Scuseria, G. E.; Tao, J.; Perdew, J. P. Erratum: “Comparative assessment of a new nonempirical density functional: Molecules and hydrogen-bonded complexes” [J. Chem. Phys. 119, 12129 (2003)]. *J. Chem. Phys.* **2004**, *121* (22). DOI: https://doi.org/10.1063/1.1795692

(87) Tao, J.; Perdew, J. P.; Staroverov, V. N.; Scuseria, G. E. Climbing the density functional ladder: nonempirical meta-generalized gradient approximation designed

for molecules and solids. *Phys. Rev. Lett.* **2003**, *91* (14), 146401. DOI: https://doi.org/10.1103/PhysRevLett.91.146401

(88) Grimme, S.; Antony, J.; Ehrlich, S.; Krieg, H. A consistent and accurate ab initio parametrization of density functional dispersion correction (DFT-D) for the 94 elements H-Pu. *J. Chem. Phys.* **2010**, *132* (15), 154104. DOI: https://doi.org/10.1063/1.3382344

(89) Grimme, S. Semiempirical GGA-type density functional constructed with a long-range dispersion correction. *J. Comput. Chem.* **2006**, *27* (15), 1787-1799. DOI: https://doi.org/10.1002/jcc.20495

(90) Neese, F.; Wennmohs, F.; Hansen, A.; Becker, U. Efficient, approximate and parallel Hartree–Fock and hybrid DFT calculations. A 'chain-of-spheres' algorithm for the Hartree–Fock exchange. *Chem. Phys.* **2009**, *356* (1-3), 98-109. DOI: https://doi.org/10.1016/j.chemphys.2008.10.036

(91) Izsak, R.; Neese, F. An overlap fitted chain of spheres exchange method. *J. Chem. Phys.* **2011**, *135* (14), 144105. DOI: https://doi.org/10.1063/1.3646921

(92) Pantazis, D. A.; Neese, F. All-Electron Scalar Relativistic Basis Sets for the Actinides. *J. Chem. Theory. Comput.* **2011**, *7* (3), 677-684. DOI: https://doi.org/10.1021/ct100736b

(93) Weigend, F.; Ahlrichs, R. Balanced basis sets of split valence, triple zeta valence and quadruple zeta valence quality for H to Rn: Design and assessment of accuracy. *Phys. Chem. Chem. Phys.* **2005**, *7* (18), 3297-3305. DOI: https://doi.org/10.1039/B508541A

(94) Weigend, F. Accurate Coulomb-fitting basis sets for H to Rn. *Phys. Chem. Chem. Phys.* **2006**, *8* (9), 1057-1065. DOI: https://doi.org/10.1039/B515623H

(95) Becke, A. D. Density‐functional thermochemistry. III. The role of exact exchange. *J. Chem. Phys.* **1993**, *98* (7), 5648-5652. DOI: https://doi.org/10.1063/1.464913

(96) Yanai, T.; Tew, D. P.; Handy, N. C. A new hybrid exchange–correlation functional using the Coulomb-attenuating method (CAM-B3LYP). *Chem. Phys. Lett.* **2004**, *393* (1-3), 51-57. DOI: https://doi.org/10.1016/j.cplett.2004.06.011

(97) Ernzerhof, M.; Scuseria, G. E. Assessment of the Perdew–Burke–Ernzerhof exchange-correlation functional. *J. Chem. Phys.* **1999**, *110* (11), 5029-5036. DOI: https://doi.org/10.1063/1.478401

(98) Perdew, J. P.; Burke, K.; Ernzerhof, M. Generalized Gradient Approximation Made Simple. *Phys. Rev. Lett.* **1996**, *77* (18), 3865-3868. DOI: https://doi.org/10.1103/PhysRevLett.77.3865

(99) Perdew, J. P.; Ernzerhof, M.; Burke, K. Rationale for mixing exact exchange with density functional approximations. *J. Chem. Phys.* **1996**, *105* (22), 9982-9985. DOI: https://doi.org/10.1063/1.472933

(100) Adamo, C.; Barone, V. Toward reliable density functional methods without adjustable parameters: The PBE0 model. *J. Chem. Phys.* **1999**, *110* (13), 6158-6170. DOI: https://doi.org/10.1063/1.478522

(101) Grimme, S. Accurate calculation of the heats of formation for large main group compounds with spin-component scaled MP2 methods. *J. Phys. Chem. A* **2005**, *109* (13), 3067-3077. DOI: https://doi.org/10.1021/jp050036j

(102) Pantazis, D. A.; Chen, X. Y.; Landis, C. R.; Neese, F. All-Electron Scalar Relativistic Basis Sets for Third-Row Transition Metal Atoms. *J. Chem. Theory. Comput.* **2008**, *4* (6), 908-919. DOI: https://doi.org/10.1021/ct800047t

(103) Rolfes, J. D.; Neese, F.; Pantazis, D. A. All-electron scalar relativistic basis sets for the elements Rb-Xe. *J. Comput. Chem.* **2020**, *41* (20), 1842-1849. DOI: https://doi.org/10.1002/jcc.26355

(104) Pantazis, D. A.; Neese, F. All-Electron Scalar Relativistic Basis Sets for the Lanthanides. *J. Chem. Theory. Comput.* **2009**, *5* (9), 2229-2238. DOI: https://doi.org/10.1021/ct900090f

(105) Noro, T.; Sekiya, M.; Koga, T. Segmented contracted basis sets for atoms H through Xe: Sapporo-(DK)-*n*ZP sets (*n* = D, T, Q). *Theor. Chem. Acc.* **2012**, *131* (2), 1124. DOI: https://doi.org/10.1007/s00214-012-1124-z

(106) Aravena, D.; Neese, F.; Pantazis, D. A. Improved Segmented All-Electron Relativistically Contracted Basis Sets for the Lanthanides. *J. Chem. Theory. Comput.* **2016**, *12* (3), 1148-1156. DOI: https://doi.org/10.1021/acs.jctc.5b01048

(107) Li Manni, G.; Fdez. Galván, I.; Alavi, A.; Aleotti, F.; Aquilante, F.; Autschbach, J.; Avagliano, D.; Baiardi, A.; Bao, J. J.; Battaglia, S.; Birnoschi, L.; Blanco-González, A.; Bokarev, S. I.; Broer, R.; Cacciari, R.; Calio, P. B.; Carlson, R. K.; Carvalho Couto, R.; Cerdán, L.; Chibotaru, L. F.; Chilton, N. F.; Church, J. R.; Conti, I.; Coriani, S.; Cuéllar-Zuquin, J.; Daoud, R. E.; Dattani, N.; Decleva, P.; de Graaf, C.; Delcey, M. G.; De Vico, L.; Dobrautz, W.; Dong, S. S.; Feng, R.; Ferré, N.; Filatov, M.; Gagliardi, L.; Garavelli, M.; González, L.; Guan, Y.; Guo, M.; Hennefarth, M. R.; Hermes, M. R.; Hoyer, C. E.; Huix-Rotllant, M.; Jaiswal, V. K.; Kaiser, A.; Kaliakin, D. S.; Khamesian, M.; King, D. S.; Kochetov, V.; Krośnicki, M.; Kumaar, A. A.; Larsson, E. D.; Lehtola, S.; Lepetit, M.-B.; Lischka, H.; López Ríos, P.; Lundberg, M.; Ma, D.; Mai, S.; Marquetand, P.; Merritt, I. C. D.; Montorsi, F.; Mörchen, M.; Nenov, A.; Nguyen, V. H. A.; Nishimoto, Y.; Oakley, M. S.; Olivucci, M.; Oppel, M.; Padula, D.; Pandharkar, R.; Phung, Q. M.; Plasser, F.; Raggi, G.; Rebolini, E.; Reiher, M.; Rivalta, I.; Roca-Sanjuán, D.; Romig, T.; Safari, A. A.; Sánchez-Mansilla, A.; Sand, A. M.; Schapiro, I.; Scott, T. R.; Segarra-Martí, J.; Segatta, F.; Sergentu, D.-C.; Sharma, P.; Shepard, R.; Shu, Y.; Staab, J. K.; Straatsma, T. P.; Sørensen, L. K.; Tenorio, B. N. C.; Truhlar, D. G.; Ungur, L.; Vacher, M.; Veryazov, V.; Voß, T. A.; Weser, O.; Wu, D.; Yang, X.;

Yarkony, D.; Zhou, C.; Zobel, J. P.; Lindh, R. The OpenMolcas Web: A Community-Driven Approach to Advancing Computational Chemistry. *J. Chem. Theory. Comput.* **2023**, *19* (20), 6933-6991. DOI: https://doi.org/10.1021/acs.jctc.3c00182

(108) Roos, B. O.; Lindh, R.; Malmqvist, P.-Å.; Veryazov, V.; Widmark, P.-O. Main Group Atoms and Dimers Studied with a New Relativistic ANO Basis Set. *J. Phys. Chem. A* **2004**, *108* (15), 2851-2858. DOI: https://doi.org/10.1021/jp031064+

(109) Roos, B. O.; Veryazov, V.; Widmark, P.-O. Relativistic atomic natural orbital type basis sets for the alkaline and alkaline-earth atoms applied to the ground-state potentials for the corresponding dimers. *Theor. Chem. Acc.* **2004**, *111* (2), 345-351. DOI: https://doi.org/10.1007/s00214-003-0537-0

(110) Roos, B. O.; Lindh, R.; Malmqvist, P.-Å.; Veryazov, V.; Widmark, P.-O. New Relativistic ANO Basis Sets for Transition Metal Atoms. *J. Phys. Chem. A* **2005**, *109* (29), 6575-6579. DOI: https://doi.org/10.1021/jp0581126

(111) Roos, B. O.; Lindh, R.; Malmqvist, P.-Å.; Veryazov, V.; Widmark, P.-O. New relativistic ANO basis sets for actinide atoms. *Chem. Phys. Lett.* **2005**, *409* (4), 295-299. DOI: https://doi.org/10.1016/j.cplett.2005.05.011

(112) Reiher, M. Douglas–Kroll–Hess Theory: a relativistic electrons-only theory for chemistry. *Theor. Chem. Acc.* **2006**, *116* (1), 241-252. DOI: https://doi.org/10.1007/s00214-005-0003-2

(113) Li Manni, G.; Carlson, R. K.; Luo, S.; Ma, D.; Olsen, J.; Truhlar, D. G.; Gagliardi, L. Correction to Multiconfiguration Pair-Density Functional Theory. *J. Chem. Theory. Comput.* **2016**, *12* (1), 458-458. DOI: https://doi.org/10.1021/acs.jctc.5b01182

(114) Li Manni, G.; Carlson, R. K.; Luo, S.; Ma, D.; Olsen, J.; Truhlar, D. G.; Gagliardi, L. Multiconfiguration Pair-Density Functional Theory. *J. Chem. Theory. Comput.* **2014**, *10* (9), 3669-3680. DOI: https://doi.org/10.1021/ct500483t